HHS Public Access

Author manuscript

Immunity. Author manuscript; available in PMC 2025 June 12.

Published in final edited form as:

Immunity. 2025 June 10; 58(6): 1519–1535.e11. doi:10.1016/j.immuni.2025.04.007.

Inflammasome signaling in astrocytes modulates hippocampal plasticity

Kristine E. Zengeler[1,*], **Ava Hollis**[1], **Tyler C.J. Deutsch**[2], **Joshua D. Samuels**[1,3,4], **Hannah Ennerfelt**[5], **Katelyn A. Moore**[1], **Eric J. Steacy**[1], **Vikram Sabapathy**[6], **Rahul Sharma**[6], **Manoj K. Patel**[2,3], **John R. Lukens**[1,3,7,*]

[1]Center for Brain Immunology and Glia (BIG), Department of Neuroscience, University of Virginia, Charlottesville, VA 22908, USA

[2]Department of Anesthesiology, University of Virginia, Charlottesville, VA 22908, USA

[3]Neuroscience Graduate Program, University of Virginia, Charlottesville, VA 22908, USA

[4]Department of Biomedical Engineering, University of Virginia, Charlottesville, VA 22908, USA

[5]Department of Neurology and Neurological Sciences, Stanford University, Palo Alto, CA 24304, USA

[6]Division of Nephrology, Department of Medicine, Center for Immunity, Inflammation and Regenerative Medicine (CIIR), University of Virginia, Charlottesville, VA 22908, USA

[7]Lead contact

SUMMARY

Emerging evidence indicates that a baseline level of controlled innate immune signaling is required to support proper brain function. However, little is known about the function of most innate immune pathways in homeostatic neurobiology. Here, we report a role for astrocyte-dependent inflammasome signaling in regulating hippocampal plasticity. Inflammasomes are multiprotein complexes that promote caspase-1-mediated interleukin (IL)-1 and IL-18 production in response to pathogens and tissue damage. We observed that inflammasome complex formation was regularly detected under homeostasis in hippocampal astrocytes and that its assembly is dynamically regulated in response to learning and regional activity. Conditional ablation of caspase-1 in astrocytes limited hyperexcitability in an acute seizure model and impacted hippocampal plasticity via modulation of synaptic protein density, neuronal activity, and perineuronal net coverage. Caspase-1 and IL-18 regulated hippocampal IL-33 production and

*Correspondence: kez9hf@virginia.edu (K.E.Z.), jrl7n@virginia.edu (J.R.L.).

AUTHOR CONTRIBUTIONS

K.E.Z. and J.R.L. designed the study. K.E.Z., A.H., J.D.S., and H.E. performed experiments. K.E.Z. performed bioinformatics analyses. T.C.J.D. performed electrophysiological experiments, and M.K.P. provided electrophysiological experimental advice, oversight, and interpretation. K.E.Z. analyzed data. K. A.M. and E.J.S. oversaw animal husbandry and conducted genotyping. V.S. and R.S. generated $Il33^{fl/fl}$ mice. K.E.Z. and J.R.L. wrote the manuscript. J. R.L. oversaw the project.

DECLARATION OF INTERESTS

R.S. has equity and consultancy interests in Slate Bio Inc.

SUPPLEMENTAL INFORMATION

Supplemental information can be found online at https://doi.org/10.1016/j.immuni.2025.04.007.

related plasticity. These findings reveal a homeostatic function for astrocyte inflammasome activity in regulating hippocampal physiology in health and disease.

In brief

The function of immune pathways in homeostatic neurobiology remains underexplored. Zengeler et al. find that the inflammasome complex, typically associated with immune responses, is involved in memory-related and seizure processes in the adult murine brain. These findings shed light on systems that could be impacted in several neurologic disease states involving inflammasome dysfunction or therapeutic targeting.

Graphical Abstract

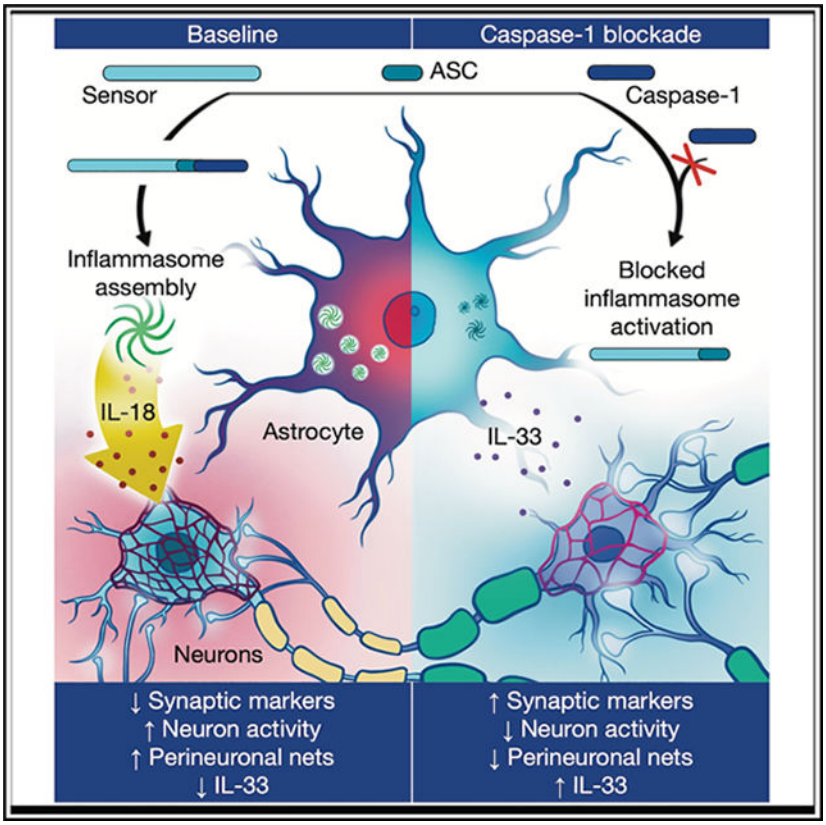

INTRODUCTION

Precise control over synaptic connections underlies the capability of neurons to modify circuit processing throughout the lifetime of an organism. A given experience activates and induces dynamic modification in hippocampal physiology, imparting this brain region with the ability to encode experiences as memories. Consequently, impaired hippocampal synaptic plasticity is associated with deficits in memory storage and has been linked to a myriad of neurologic disease states such as Alzheimer's disease and dementia. On the other hand, hyperactivation of hippocampal circuitry also contributes to seizures, which are

debilitating neurological events characterized by excessive neuronal activity and involuntary movements.

Immune signaling in the brain has received growing attention as a major contributor to various forms of neurological disease. Emerging evidence indicates that immune molecules and pathways can also be exploited to support physiologic brain development and function.[1–4] For example, the alarmin interleukin (IL)-33 is typically released upon cell damage and acts in a pro-inflammatory manner in infection, allergy, and cancer.[5] Yet, IL-33 is also necessary for hippocampal synaptic plasticity.[6–8] Despite growing appreciation for this dichotomous role of IL-33, little is currently known about the molecular pathways that regulate hippocampal IL-33 levels.

The inflammasome is a multiprotein signaling complex, assembled following detection of intracellular danger signals, that contributes to innate immune responses.[9–11] Inflammasome assembly canonically leads to cleavage and release of pro-in-flammatory cytokines such as IL-1β and IL-18 as well as cell lysis, together constituting pyroptotic cell death.[12,13] The inflammasome has more recently been recognized to contribute to immune activation in sterile contexts within the central nervous system (CNS), including neurodegenerative diseases, stroke, depression, and more.[14–17] Inflammasome-associated cytokines including IL-1β and IL-18 have also been shown to modulate hippocampal long-term potentiation (LTP) and correlate with hippocampal hyperexcitability in epilepsy.[18–23]

In this study, we report that the inflammasome is activated in the healthy adult brain and contributes to homeostatic CNS cell function. We find that astrocyte-specific caspase-1 blockade impacts multiple measures of hippocampal plasticity including transcriptional landscape, synaptic protein density, neuronal activity, perineuronal net (PNN) abundance, and IL-33 production. Leveraging the ability of the inflammasome to modulate neuronal activity, we find that astrocyte-specific deletion of caspase-1 protects mice from severe hippocampal hyperexcitability-driven seizures. These findings reveal an important role for astrocyte-intrinsic inflammasome signaling in modulating hippocampal biology in both healthy and hyperexcitable contexts.

RESULTS

Inflammasome-associated ASC speck formation is dynamically regulated in the healthy adult brain

Canonically, the inflammasome consists of a cytosolic innate immune sensor and caspase-1 which oligomerize with an adaptor bridging molecule, ASC, upon obligate ligand recognition by the sensor.[9–11] The ASC^{Citrine} reporter mouse provides for *in situ* localization of active inflammasome assembly, as diffuse ASC becomes aggregated into bright ASC specks upon oligomerization into multimeric complexes.[24] We noticed the presence of ASC specks throughout the brain in healthy adult mice (Figure 1A). ASC specks were highly concentrated within the hippocampus, cerebellum, and cortex, with lower but still substantial numbers distributed throughout the brain including the nucleus accumbens, substantia nigra, and olfactory bulb (Figures 1B and 1C).

Inflammasomes come in a variety of subtypes, providing a platform to sense a broad spectrum of intracellular danger signals.[9–11] Sensors bridged to an effector caspase (typically, caspase-1) in this manner then trigger caspase autocatalytic cleavage.[9–11] We wondered which, if any, inflammasome sensors were expressed in the adult mouse brain under homeostatic conditions. We found that the sensors AIM2, NLRP1, NLRP2, and NLRP3 were all present in lysates from microdissected hippocampus, cerebellum, and cortex of wild-type (WT) mice (Figures S1A and S1B). Sensor expression corresponded with ASC dimerization and caspase-1 cleavage in these three brain regions (Figures 1D and 1E).

The most well-known inflammasome targets include cytokines, such as pro-IL-1β and pro-IL-18, which require cleavage to elicit their pro-inflammatory signaling properties.[9–11] We noted the presence of both pro-IL-1β and pro-IL-18 in hippocampus, cerebellum, and cortex lysates, but we only detected the cleaved active signaling version of IL-18, and we did not detect cleaved IL-1β (Figures 1D and 1E). Notably, caspase-1 and IL-18 concentrations were highest in the hippocampus, consistent with our ASC speck imaging findings (Figures 1A–1C).

Inflammasomes can also cleave gasdermin-D (GSDMD), of which the N-terminal fragment can self-oligomerize creating pores in the plasma membrane that can cause cell lysis.[25] We noted the presence of canonical full-length GSDMD exclusively in the cerebellum of adult WT mice (Figures S1A and S1B). While we failed to see canonical 53 kDa GSDMD in either the hippocampus or cortex, we did note the presence of larger 75 kDa bands across all three regions assessed, in addition to a very large 150 kDa band in the cerebellum alone (Figures S1A and S1B). Yet, cleaved 29 kDa GSDMD was not detected in any of the regions assessed. These findings suggest that there might be a non-canonical role of GSDMD in the cerebellum and that there is a lack of baseline hippocampal GSDMD engagement. Inflammasome assembly is typically associated with activation of the transcription factor nuclear factor κB (NF-κB) which promotes sensor and cytokine expression.[26] We observed phosphorylation of NF-κB and its regulator, IκBα, in adult WT mice brain lysates (Figures S1A and S1B).

A number of CNS cell activity stimuli, including ATP, extracellular Ca^{2+}, reactive oxygen species (ROS) production, and K^+ fluxes, are known to modulate inflammasome activation.[14,27] We therefore postulated that one influence of homeostatic CNS inflammasome assembly could be cell activity. To address this question, we turned to an *ex vivo* system to track inflammasome assembly by ASC fluorescence (Figure 1F). We plated primary $ASC^{Citrine}$ CNS cells and measured relative fluorescence over time in response to $CaCl_2$, which is known to induce calcium-related activity broadly across multiple CNS cell types.[28–31] Non-treated (NT) cells served as a negative control. As a positive control, we treated cells with etoposide, which has been shown to trigger inflammasome activation in CNS cells.[32] We observed that etoposide treatment induced a rapid increase in ASC fluorescence indicative of inflammasome assembly in our *ex vivo* setup (Figure S1C). In contrast, $ASC^{Citrine}$ fluorescence was significantly reduced after 1 h of $CaCl_2$ exposure (Figures 1G and 1H). Reduced inflammasome assembly continued in this manner out to 6 h of continuous $CaCl_2$ treatment (Figures 1G and 1H). Assembly was reduced over 50%

during this time frame (Figure 1H). We next wondered whether this effect was reversible. To test this, we washed out $CaCl_2$ after the 6 h window and found that ASC fluorescence recovered to pre-treatment levels (Figure 1G, time 18 h). While etoposide may induce irreversible inflammasome assembly and cell death as previously reported in CNS cells,[32] our findings suggest that cell activation with $CaCl_2$ can lead to reversible inflammasome dampening in CNS cells.

We next sought to further investigate the connection between CNS cell activity and inflammasome assembly in an *in vivo* physiologic setting. Given the high density of ASC specks observed in the hippocampus at homeostasis (Figures 1A–1C), we wondered whether engagement of this brain region would modulate inflammasome assembly. Environmental enrichment (EE) is well characterized to activate hippocampal neurons and promote synaptic plasticity.[33–38] We found that exposing $ASC^{Citrine}$ mice to EE significantly attenuated hippocampal ASC speck numbers (Figures 1I and 1J). This phenomenon of reduced inflammasome assembly occurred after just 48 h of EE and persisted out to a full week of EE (Figure S1D).

EE also reduced whole brain gene expression of the inflammasome sensor *Nlrp3* and cytokine *Il1b* (Figure S1E). We noted that this phenomenon was accompanied by a reduction in markers of gliosis including IBA1 (Figures S1F and S1G), GFAP (Figures S1H and S1I), and S100β (Figures S1J and S1K) in the hippocampus. Moreover, inflammasome assembly was coordinately lowered across hippocampal subregions in response to EE (Figure S1L). Hippocampal aging is also known to diminish synapse numbers, synaptic plasticity, and learning and memory function.[39,40] As opposed to EE, we found that hippocampal ASC speck numbers increased with age (Figures 1K, 1L, S1M, and S1N). This increase in inflammasome assembly with age was also noted in the cerebellum (Figures S1O and S1P).

We next sought to assess the involvement of inflammasome assembly in the hippocampus as it directly relates to the processes of learning and memory. To this end, we utilized the Morris water maze (MWM) in which mice learn to locate an escape platform submerged beneath opaque water using spatial cues. We trained $ASC^{Citrine}$ mice on this hippocampus-dependent spatial learning task and then assessed memory using a probe trial in which the platform is removed. Control $ASC^{Citrine}$ mice underwent the same protocol including swim trials in the pool with spatial cues but without any hidden platform to guide learning. Mice were harvested after 2 days of training (“learn” group) or after the probe trial (“recall” group for those trained with the hidden platform or “swim” group for controls) (Figure 1M). We found that spatial task learning and escape location recall both significantly reduced ASC speck numbers relative to controls (Figures 1N and 1O). Notably, this effect was unique to the hippocampus, the key region engaged in this spatial task, as cerebellum numbers of ASC specks were unchanged after spatial memory recall (Figures S1Q and S1R). These results reveal that active engagement of the hippocampus in a learning or memory recall task is sufficient to dampen inflammasome assembly.

Finally, we wondered whether modulation of inflammasome assembly via brain region engagement was a phenomenon specific to the hippocampus. To this end, we leveraged the cerebellum-dependent motor learning rotarod task in which mice are trained to run on a

rotating rod over consecutive trials (Figures S1S–S1U). We found that motor engagement alone after just a single trial significantly dampened inflammasome assembly in the cerebellum, while motor memory recall significantly increased ASC speck numbers (Figures S1V and S1W). These data point toward activity-related inflammasome modulation in the cerebellum that is likely distinct from the processes engaged in the hippocampus. Altogether, we uncovered that inflammasome assembly is dynamically regulated in the adult brain in response to environmental perturbations.

Blocking inflammasome function alters hippocampal plasticity

We next sought to more functionally assess whether inflammasome activation influences hippocampal physiology. Neurons compete for integration into memory networks and are preferentially recruited into these mnemonic traces based on their relative activity levels, with more active neurons typically winning.[41] Network sparsity is thought to correlate with sharpened memory, as non-specific neuronal activation worsens memory recall.[41–43] We initially wondered whether inflammasome signaling directly impacts neuronal activity. To test this, we leveraged c-Fos$^{Cre\text{-}ERT2}$ LSL-tdTomato mice (denoted as TRAP2;tdTomato hereafter) in which activated neurons can be fluorescently marked in a time-controlled manner. Given that caspase-1 is a central effector component of the majority of inflammasomes, we chose to inhibit caspase-1 to block downstream target cleavage using the blood-brain barrier penetrant caspase-1 inhibitor, VX765.[44,45]

We injected TRAP2;tdTomato mice with VX765 or vehicle as a control prior to tamoxifen administration, and then exposed these mice to a novel EE to induce hippocampal neuronal activity in a physiological manner (Figure 2A). As expected, 48 h EE exposure induced hippocampal neuron activity that was fluorescently trapped in TRAP2;tdTomato mice (Figure 2B). Trapped tdTomato+ cells appeared neuronal by morphology and did not colocalize with GFAP, which stains hippocampal astrocytes at baseline (Figure S2A). VX765 treatment significantly reduced hippocampal tdTomato+ trapped signal (Figures 2B and 2C) corresponding to fewer trapped neurons (Figures 2B and 2D) compared with vehicle controls. This effect extended to other regions involved in hippocampal circuitry, including the subiculum and cortical regions (Figures S2B–S2D). Thus, we find that blocking inflammasome activation is sufficient to dampen physiologic neuronal activity. These data paired with our previous findings that cell activity can influence inflammasome assembly in CNS cells (Figures 1F–1H) suggest that cell activity and inflammasome assembly might exist in a feedback loop.

Neuronal synaptic plasticity, encompassing synaptic rearrangement and stabilization following a stimulus, is an obligatory process allowing for the formation of new neuronal connections during memory formation.[46–48] We next queried whether the abundance of synaptic structures may be affected by the inflammasome. The Thy1^{YFP} reporter mouse allows for the assessment of neuronal morphology by virtue of its sparse labeling of neurons throughout the brain. We treated adult Thy1^{YFP} mice with VX765 or vehicle control and then assessed synaptic spine density. We found that mice treated with VX765 had a significantly higher density of spines in both the hippocampus (Figures 2E and 2F) and cortex (Figures 2G and 2H). Given the increase in post-synaptic spines, we wondered

whether presynaptic terminals were coordinately impacted by caspase-1 inhibition. We found a significant increase in the presynaptic protein synaptophysin in hippocampal lysates from VX765-treated mice (Figures 2I and 2J). We confirmed this result through immunohistochemistry in which we observed significantly more synaptophysin puncta in the CA1 hippocampal subregion of VX765-treated mice (Figures 2K and 2L).

Finally, we sought to further investigate the characteristics of synapses impacted by blocking inflammasome function. The glutamate transporter VGLUT1 is present in presynaptic terminals and is argued to also be functional in astrocytes at glutamatergic synapses.[49–51] We found that hippocampal VGLUT1 was heightened in VX765-treated mice (Figures 2I and 2M). Inspired by our findings that blocking caspase-1 attenuated neuronal activity, we assessed hippocampal $GABA_AR\alpha1$, a receptor enriched on post-synaptic inhibitory terminals. We found a significant enrichment for $GABA_AR\alpha1$ in mice treated with VX765 (Figures 2I and 2N). These collective results illustrate that blocking inflammasome activity can alter aspects of synaptic structures in the hippocampus.

Inflammasome activity in astrocytes regulates hippocampal plasticity

Inflammasome activation has primarily been witnessed in peripheral immune cells in response to pathogens.[9,10] Similarly, states of sterile CNS pathology have also been linked to inflammasome activation in the brain-resident immune cells, microglia.[14,15] We next sought to determine the cellular location of inflammasomes in the homeostatic adult hippocampus and cerebellum. Assembled inflammasomes in the hippocampus were found primarily in astrocytes (GFAP+ cells) rather than microglia (IBA1+ cells; Figures 3A, 3B, S2E, and S2F). These ASC+ GFAP+ cells were bona fide astrocytes, rather than neural precursors, as confirmed by colocalization using the astrocyte marker S100β (Figure S2G). We also confirmed that this localization was not purely a product of the $ASC^{Citrine}$ reporter line by using an antibody against ASC in WT mice (Figure S2H). Using this ASC antibody, we also noticed assembled inflammasomes within some Thy1+ neurons, though to a much lesser extent than that of astrocytes (Figures S2H–S2J).

Meanwhile in the cerebellum, ASC specks were predominantly found in the soma and dendrites of Calbindin+ Purkinje cells (Figure S2K). We noted that Purkinje cells in the healthy cerebellum also expressed the inflammasome cleavage target GSDMD (Figure S2K), tracking with our western blot findings (Figures S1A and S1B). In all, these data reveal that baseline inflammasome assembly in the adult brain is cell-type specific in a regional manner.

Throughout our studies, we observed variation in the size and morphology of ASC specks in $ASC^{Citrine}$ mice. In the hippocampus, ASC specks appeared as smaller prototypical specks, mid-sized “splotch-like” formations, and larger “spindle-like” structures (Figures S2L and S2M). Each of these variations were found inside CA1 astrocytes (Figure S2N). Inflammasome-initiated active cytokine release and cell lysis constitutes a pro-inflammatory type of cell death known as pyroptosis.[12,13] Therefore, we next sought to evaluate whether astrocytes in inflammasome-rich regions were dying. We conducted the TUNEL assay and propidium iodide (PI) staining in concert with visualizing ASC specks but failed to witness any cells, including astrocytes, that were positive for these cell death markers in the healthy

adult hippocampus (Figures S3A–S3F). Notably, ESCRT-III-mediated membrane repair can both limit and uncouple events downstream of inflammasome activation to ultimately allow for cytokine release without cell death.[52–55] We speculate that astrocytes activating the inflammasome are able to avoid pyroptosis while still engaging other inflammasome signaling pathways, such as active cytokine release.

We decided to further investigate the involvement of inflammasomes in hippocampal astrocytes, given the sensitivity of hippocampal inflammasomes to physiological environmental alterations (Figures 1I–1O) and involvement in neuronal plasticity (Figure 2). To functionally probe the importance of astrocyte inflammasome activation, we generated $Casp1^{fl/fl}$;$Aldh1l1^{Cre\text{-}ERT2}$ mice (hereafter referred to as $Casp1^{\Delta Ast}$). We fed tamoxifen food to $Casp1^{\Delta Ast}$ and Cre-negative littermate control mice (hereafter referred to as $Casp1^{cont}$) upon weaning to genetically ablate caspase-1 function following neurodevelopment in adult astrocytes. Mice were then returned to regular food for the remainder of the experiment. We confirmed astrocyte-specific loss of *Casp1* expression in these animals (Figures S3G and S3H).

We wondered whether the increase in synaptic marker density resulting from widespread caspase-1 inhibition (Figures 2E–2N) was cell intrinsic to neurons or whether it could be a downstream consequence of inflammasome activation within astrocytes. Thus, we assessed hippocampal synaptic markers in our $Casp1^{\Delta Ast}$ mice. In line with our findings from caspase-1-inhibitor-treated mice, synaptophysin was significantly increased, and we observed a trend toward increased VGLUT1 alongside significantly increased $GABA_AR\alpha1$ protein in $Casp1^{\Delta Ast}$ mice compared with controls by western blot (Figures 3C–3F). These immunoblot findings were further confirmed by immunohistochemistry (Figures 3G, 3H, S3I, and S3J). We also noted that the number of colocalized puncta between presynaptic/astrocytic VGLUT1 with post-synaptic Homer-1 was increased upon caspase-1 ablation in astrocytes (Figures 3I and 3J) concomitant with an increase in Homer-1 alone (Figures S3K and S3L). These results together suggest that some synaptic markers can be regulated by astrocyte inflammasome activity.

Whether these changes to hippocampal synapses driven by astrocyte caspase-1 is sufficient to alter neuron network activity remained a question. To interrogate this, we stained for the immediate-early gene c-Fos, which is substantially upregulated following the induction of neuron activity. In line with our pharmacologic studies (Figures 2A–2D), we observed a significant decrease in c-Fos+ cell numbers in the hippocampus of $Casp1^{\Delta Ast}$ mice compared with controls (Figures 3K and 3L). The majority of the c-Fos+ hippocampal cells in these experiments were neurons rather than astrocytes (Figure S3M).

We wondered why neuronal activity was decreased upon blocking inflammasome function even though we observed a seeming increase in synaptic abundance, which might suggest potentiated hippocampal drive. To more definitively assess hippocampal neuronal function in our $Casp1^{\Delta Ast}$ mice, we conducted slice electrophysiology in these animals and Cre-negative littermate controls. We performed patch-clamp electrophysiology recordings of CA1 pyramidal neurons and noted a significant attenuation of intrinsic firing upon loss of astrocyte caspase-1 (Figures 3M and 3N). Neurons from $Casp1^{\Delta Ast}$ mice exhibited

progressive action potential failure at current injection steps between 400 and 600 pA (Figures 3M and 3N). Analysis of membrane and action potential properties revealed no difference in the membrane or action potential properties of CA1 pyramidal neurons (Table S1). These data suggest that caspase-1 activity in astrocytes is required to achieve proper neuronal firing in the hippocampus.

Caspase-1 signaling in hippocampal astrocytes influences memory-related gene expression

We next wondered how inflammasomes within astrocytes could support neuronal physiology in the hippocampus on a more mechanistic level. To explore this, we first decided to take an unbiased approach by conducting single-cell RNA sequencing (scRNA-seq) of hippocampi pooled from Casp1$^{\Delta Ast}$ mice and Cre-negative controls (n = 3 mice per group). After quality control and filtering, 28,308 total cells were used for downstream analysis. T-distributed stochastic neighbor embedding (tSNE) clustering revealed 16 distinct cell populations distributed across both genotypes (Figures 4A and S3N). We identified each cell cluster using top cluster-enriched genes and cell-specific markers and found that large populations of astrocytes, oligodendrocytes, and microglia were recovered among other cell types in both groups (Figures 4A and S3O–S3Q).

We first conducted a pseudobulk differential expression analysis (DEA) on all cells and found 166 differentially expressed genes (DEGs) between Casp1^{cont} and Casp1$^{\Delta Ast}$ hippocampi (Figure S3R). We noticed that many of these DEGs were related to learning and memory, including *Jun*, *Fos*, *Snap25*, *Npy*, and *Mbp*. This was reflected in Gene Ontology (GO) pathway analysis conducted on upregulated and downregulated genes. Genes related to synaptic compartments and the myelin sheath (Figure 4B) that corresponded with memory-related pathways such as “learning,” “synaptic signaling,” “cognition,” and “neurogenesis” (Figure 4C) were all upregulated. We noted downregulation of the transcription factor AP-1 complex (Figure 4B), which verified our functional studies that c-Fos protein was reduced in Casp1$^{\Delta Ast}$ hippocampi (Figures 3K and 3L). We also found the reduction in AP-1 complex notable given that the inflammasome-derived cytokines IL-1β and IL-18 are known to drive AP-1 complex transcription.[56]

We next examined each major cluster to reveal cell-type-specific changes following the loss of caspase-1 in astrocytes. The 11,408 astrocytes were subclustered and labeled via pathway analyses and manual investigation of cluster-enriched genes. The largest subclusters were homeostatic and synaptogenesis-promoting astrocytes and smaller subclusters expressed plasticity-related genes and markers of subventricular zone astrocytes (Figures S4A–S4C). Every astrocyte subcluster was found in both experimental groups with only a moderate shift away from synaptogenic into homeostatic astrocytes occurring in Casp1$^{\Delta Ast}$ hippocampi (Figure S4B).

Within astrocytes, we identified 82 genes to be significantly differentially expressed between Casp1$^{\Delta Ast}$ and control cells (Figure S4D) and pathways related to metabolic responses and cell differentiation were found to be downregulated (Figure S4E). We examined the relative enrichment of DEGs distributed across each astrocyte subcluster and observed no particular coalescence upon a specific subcluster (Figure S4F). We wondered whether the

decrease in metabolism-related gene expression would alter astrocyte activity. While total cell and astrocyte numbers were unchanged (Figures S4G–S4I) as well as the total coverage of GFAP (Figures S4G and S4J), we did note increased coverage of S100β in Casp1$^{\Delta Ast}$ mice (Figures S4K and S4L). Altogether, these transcriptional and histologic findings reveal that astrocytes largely tolerate the loss of caspase-1 across these baseline measures. We speculate that the changes to hippocampal physiology observed after astrocyte caspase-1 ablation may largely stem from post-transcriptional processes within astrocytes, for instance, caspase-1-dependent cytokine activation and release.

We also sought to determine whether astrocyte caspase-1 deficiency impacted gene expression in other hippocampal cell types. We found a number of DEGs within microglia, as well as a few in oligodendrocytes, endothelial cells, and choroid plexus cells (Figures S4M–S4U). These data collectively demonstrate a coordinated transcriptional response by many hippocampal cell types dependent upon astrocyte caspase-1 that could influence memory-related processes.

Inflammasome signaling in astrocytes modulates hippocampal function, neurogenesis, and PNN formation

Given that caspase-1 blockade was sufficient to alter multiple aspects of hippocampal plasticity, we next sought to functionally probe the importance of astrocyte inflammasomes on mouse behavior. To this end, we conducted fear conditioning and then repeatedly conducted recall tests to assess long-term memory persistence (Figure 4D). We found that Casp1$^{\Delta Ast}$ mice froze significantly less than controls over consecutive context testing (Figure 4E). When assessed at a remote time point, control mice still identified the trained context as fearful compared with a novel context (Figures 4F and 4G). Meanwhile, Casp1$^{\Delta Ast}$ mice froze equally within contexts (Figures 4F and 4G), indicating that Casp1$^{\Delta Ast}$ mice are no longer able to distinguish the feared context from a novel context and may have an impairment in long-term spatial memory persistence. Importantly, these behavioral changes were unrelated to locomotion or anxiety-relate behavior (Figures S5A–S5D). These long-term memory impairments are consistent with our observation of inflammasome assembly in homeostatic physiologic states (Figures 1A–1E) as it lends to the concept that some baseline inflammasome activity contributes to normal brain function.

The production and integration of newborn neurons into hippocampal circuitry in adulthood contributes to plasticity in this region.[57,58] Our scRNA-seq pathway analyses uncovered an up-regulation of genes related to neurogenesis in the hippocampus upon astrocyte-specific caspase-1 deletion (Figure 4C). Moreover, inflammasome-derived IL-1 family cytokines are well documented to influence neurogenesis.[59] During hippocampal neurogenesis, neural progenitor cells in the dentate gyrus (DG) subregion are marked by doublecortin (DCX) expression.[60,61] We found that DCX coverage was increased in Casp1$^{\Delta Ast}$ mice across the entire DG (Figures 4H and 4I). This effect was not solely driven by an increase in cell proliferation per se, as we found equivalent numbers Ki67+ proliferating cells in the DG in Casp1$^{\Delta Ast}$ and Casp1^{cont} mice (Figures S5E and S5F). Experimentally increasing neurogenesis improves pattern separation and degrades existing information[62,63]; thus, our DCX data are consistent with the increased rate of forgetting observed in our Casp1$^{\Delta Ast}$

mice. Adult-born young neurons can activate inhibitory GABAergic circuitry, which is thought to promote neural ensemble sparsity and improve pattern separation.[62,64–66] We also observed increased $GABA_AR\alpha1$ in Casp1$^{\Delta Ast}$ animals (Figures 3E and 3F); therefore, we postulate that more immature neurons in our Casp1$^{\Delta Ast}$ mice could be one contributor to the reduced hippocampal neuron activity observed in these animals.

We next wondered what might contribute to the increased penetrance of synaptic markers observed upon caspase-1 blockade (Figures 2E–2L and 3C–3J). It has been well documented that the extracellular matrix (ECM), of which PNNs constitute a subset, is modulated following a learning experience to allow for remodeling of synapses to encode the experience as a memory.[67–69] We assessed hippocampal PNN coverage in Casp1$^{\Delta Ast}$ mice using Wisteria floribunda agglutinin (WFA) staining, a well-characterized method to fluorescently label N-acetylglucosamine components of PNNs. We found significantly reduced PNN coverage in the hippocampal CA1 region of Casp1$^{\Delta Ast}$ mice when compared with controls (Figures 4J and 4K). These collective findings were not associated with a change in total neuron coverage (Figures S5G and S5H). We speculate that reduced coverage of PNNs in Casp1$^{\Delta Ast}$ mice could provide one mechanism by which the increase in synaptic terminals in these mice might occur.

Microglia are known to influence ECM stability; therefore, we next wondered whether the loss of caspase-1 in astrocytes impacted microglial activity.[70–72] We found no change in expression of core microglia markers IBA1 and P2RY12 (Figures S5I–S5K). Yet, the phagolysosome marker CD68 was significantly heightened, corresponding to a greater number of CD68+ puncta within microglia following deletion of caspase-1 in astrocytes (Figures S5L–S5N). These findings suggest that microglial phagocytic activity might be impacted by astrocyte-intrinsic inflammasome activity and that this might contribute to some of the other hippocampal plasticity changes. In all, our findings indicate that astrocyte-dependent caspase-1 signaling can modulate multiple processes that are associated with hippocampal plasticity including neurogenesis and PNNs.

Astrocyte-intrinsic caspase-1 signaling modulates IL-33-related plasticity in the hippocampus

Recent studies have begun to uncover instrumental roles for the alarmin molecule IL-33 in hippocampal plasticity.[6,8] Hippocampal neurons primed for plasticity are enriched in IL-33, and this cytokine instructs microglial engulfment of the ECM allowing for synapse rearrangement in the adult hippocampus.[8] Given that we observed changes to synaptic markers, ECM abundance, and microglial phagolysosome activity upon deletion of caspase-1 in astrocytes, we wondered whether some of these changes might coalesce upon IL-33. We found that astrocyte-specific loss of caspase-1 significantly elevated hippocampal IL-33 expression by both total coverage and fluorescence intensity (Figures 5A–5C).

Published studies indicate that IL-33 can be produced by both hippocampal neurons and astrocytes.[6,8] We wondered whether astrocyte-specific caspase-1 deletion caused astrocytes themselves to increase IL-33 production or caused external modulation of neurons to produce more IL-33. To address this, we stained for IL-33 alongside the astrocyte marker SOX9 and neuronal marker MAP2 in Casp1$^{\Delta Ast}$ mice and Casp1^{cont} controls (Figure

5A). We noted that all nuclear IL-33 staining colocalized with nuclear SOX9 in the adult hippocampus and that diffuse IL-33 staining was within MAP2 neuronal projections (Figure 5A). We quantified colocalized areas and found that IL-33 was significantly increased in both astrocytes (SOX9+ area; Figures 5A and 5D) and neurons (MAP2+ area; Figures 5A and 5E) in Casp1$^{\Delta Ast}$ mice compared with controls. We found no change in the number of SOX9+ cells or MAP2 coverage between groups (Figures S5O–S5R).

As an additional approach to verify cell-intrinsic production of IL-33 and address potential IL-33 protein transfer between cells, we assessed neuronal and astrocytic transcriptional expression of *Il33*. To this end, we sorted neurons and astrocytes from the brains of adult Casp1$^{\Delta Ast}$ and Casp1^{cont} mice using magnetic-activated cell sorting (MACS) and then conducted qPCR on each cell fraction. We confirmed appropriate isolation by expression of canonical markers, *Slc1a2* and *Rbfox3*, in astrocyte and neuron fractions, respectively, as compared with the negative flow-through (Figures S5S and S5T). Published work has identified that adult hippocampal astrocytes express the *Il33a* isoform while neurons express the *Il33b* isoform, each of which results in the same IL-33 protein but are expressed from alternate promoters.[8] We confirmed these findings in our own sorting experiments (Figures S5U and S5V) and then assessed the relative expression of the respective enriched isoform in astrocyte and neuron fractions. We found that upon astrocyte-specific loss of caspase-1, astrocytes significantly upregulate *Il33a* (Figure 5F) and neurons significantly upregulate *Il33b* transcription (Figure 5G).

We wondered whether physiologic production of IL-33 from astrocytes might function similarly to neurons whereby it modulates spine density.[8] In addition, we were also curious to evaluate whether astrocyte-intrinsic IL-33 production might contribute to some of the caspase-1-related hippocampal plasticity changes. To address these questions, we generated astrocyte-specific IL-33 conditional knockout mice (Il33$^{fl/fl}$;Aldh1l1$^{Cre\text{-}ERT2}$ mice, hereafter referred to as Il33$^{\Delta Ast}$) and Cre-negative control littermates (hereafter referred to as Il33^{cont}). We fed these mice tamoxifen food upon weaning to induce astrocyte IL-33 deficiency (verified by immunohistochemistry; Figures S6A–S6D) and then returned them to regular food for the remainder of experiments. We first assessed the relative overlap of the synaptic markers VGLUT1 and Homer-1 in the CA1 of Il33$^{\Delta Ast}$ mice compared with Il33^{cont} mice and found a reduction in the number of colocalized puncta upon IL-33 ablation in astrocytes (Figures 5H and 5I). Meanwhile, we found no change in CA1 coverage of Synapsin1/2 or Homer-1 (Figures S6E–S6H). These findings reveal that astrocyte-intrinsic IL-33 increases glutamatergic synapse protein at baseline.

Neurons that are enriched in IL-33 also have higher expression of c-Fos, indicating that IL-33 is correlated with cell-intrinsic activity.[8] We found that a cell-extrinsic source of IL-33 also contributes to neuronal activity as our Il33$^{\Delta Ast}$ mice harbored increased CA1 c-Fos+ cell numbers compared with controls (Figures 5J and 5K). This finding suggests that astrocyte-specific IL-33 reduces the number of c-Fos+ neurons at baseline, opposite to the effects of neuron-derived IL-33,[8] which reveals a system of balance between each cellular IL-33 source. We also noted increased WFA coverage in the hippocampus of Il33$^{\Delta Ast}$ mice (Figures 5L and 5M) without impacting IBA1 coverage (Figures S6I and S6J). Collectively,

these data are consistent with the concept that heightened astrocyte IL-33 production might contribute to restrained neuronal activity and PNN coverage in our Casp1$^{\Delta As t}$ mice.

While loss of caspase-1 in astrocytes drove IL-33 production and was associated with increased synapse density, reduced neuronal activity, and diminished PNN coverage, we find that the loss of IL-33 in astrocytes has the exact opposing effects. These data argue that astrocyte-specific IL-33 could be one modulator of hippocampal physiology downstream of caspase-1. Given published findings that neuronal IL-33 contributes to hippocampal synaptic plasticity and ECM dynamics,[8] we imagine that neuron-derived IL-33 alongside astrocyte-generated IL-33 both contribute to the altered hippocampal plasticity seen with astrocyte-specific caspase-1 deletion.

IL-18 dampens IL-33 release and can be modulated by neuronal activity in the hippocampus

We next wondered what downstream inflammasome effector molecule might be responsible for the effects of caspase-1 on hippocampal plasticity in our model. Given that we detected cleaved IL-18 but not IL-1β in hippocampal lysates from adult WT mice (Figures 1D and 1E), we turned our attention to exploring a potential downstream role for IL-18 in our model. We found significantly higher IL-18 concentration in the hippocampus and cerebellum compared with the cortex of adult mice (Figure 5N), which is consistent with the higher ASC speck density and IL-18 cleavage observed in these regions (Figures 1A–1E). Upon mining our scRNA-seq data, we noted that of all the IL-1 signaling transcripts expressed in astrocytes and neurons in our dataset, *Il18* and *Il33* expression were the most pronounced (Figure S6K). Compared with all other cell types, the average expression of *Il18* was highest in the astrocyte cluster (Figures S6L–S6N). To further probe the potential for an inflammasome signaling axis in the adult hippocampus, we conducted qPCR on sorted astrocytes and neurons from adult mice. We found that *Il18* was significantly enriched in astrocytes (Figures 5O and S6O), whereas *Il18r1* was enriched in neurons (Figures 5P and S6P). We also noted *Il1b* enrichment in astrocytes (Figure S6Q). Notably, published studies find that exogenous IL-18 can influence LTP and synaptic plasticity.[22,23] Given this knowledge paired with the potential for an astrocyte IL-18 to neuron IL-18R axis, we decided to further probe IL-18 function in the adult hippocampus.

We first wondered whether IL-18 could restrain IL-33 production in the hippocampus. To this end, we isolated hippocampi from adult mice and treated primary slices for *ex vivo* study (Figure 5Q). We found that IL-18 alone was sufficient to reduce IL-33 in the hippocampus in a dose-dependent manner compared with NT control slices (Figure 5R). We also measured supernatant IL-33 concentrations and found that slices incubated with IL-18 released significantly less IL-33 compared with controls (Figure 5S), suggesting that IL-18 can restrain IL-33 release. Moreover, we observed that this result was dependent upon neuron-intrinsic IL-33 as hippocampi from neuron-specific *Il33* conditionally deleted animals (Il33$^{fl/fl}$;Cam-k2a$^{Cre-ERT2}$ mice, hereafter referred to as Il33$^{\Delta Neur}$) released similar amounts of IL-33 when treated with IL-18 as when left untreated (Figure 5S).

In our initial studies, we found that prolonged induction of neural cell activity continually suppresses inflammasome assembly and that a return to baseline activity reverses this

effect (Figures 1F–1H). We also found that EE and MWM, tasks that are beneficial for long-term memory function, dampened inflammasome assembly in the hippocampus (Figures 1I, 1J, and 1M–1O). Thus, we wondered whether the induction of physiologic neuronal activity restrains IL-18 production. To test this, we incubated hippocampus slices with modulators of neuronal activity, including forskolin (FSK) and glutamate (Figure 5Q). We found that inducing hippocampal activity with both FSK and glutamate significantly reduced hippocampal IL-18 concentrations compared with NT slices (Figures 5T and 5U). In summary, we find that the inflammasome-derived cytokine IL-18 is sufficient to dampen hippocampal IL-33 release and that induction of neuronal cell activity can restrain hippocampal IL-18 production.

Inflammasome activation propagates seizure progression

Inflammation can contribute to bouts of neuronal hyperactivity, the primary cause of seizures, as well as be a consequence of such.[73] The pro-inflammatory IL-1 cytokine family is consistently linked to many forms of epilepsy, a disorder diagnosed as having two or more seizures over one's life.[18,73] For instance, circulating IL-18 is increased in patients with epilepsy,[19] and astrocytes have been reported to heighten IL-18 production in a mouse seizure model.[20] Excessive IL-1β production is also thought to contribute to seizure-evoked excitotoxicity.[74] Our findings that caspase-1 blockade can diminish hippocampal activity inspired us to investigate whether targeting the inflammasome could be an effective method to dampen pathologic neuronal hyperactivity during seizure. To test this, we used a kainic acid (KA) model in which seizures are caused by neuronal hyperexcitability driven by glutamate receptor agonism, particularly in the hippocampus.[75,76]

We injected WT and caspase-1/-11-deficient (referred to as $Casp1^{-/-}$) mice with KA to induce seizure activity and scored seizure severity using a modified Racine scale.[77] Consistent with published studies,[73] we found that $Casp1^{-/-}$ mice were largely protected from severe seizures compared with WT controls (Figures 6A–6D). While 83% of control animals exhibited significant seizure activity following KA injection, only 44% of $Casp1^{-/-}$ animals reached this level of seizure activity. $Casp1^{-/-}$ mice had dramatically lower seizure severity over the course of scoring (Figure 6A), although the time to reach seizure onset was not impacted (Figure 6B). Indeed, $Casp1^{-/-}$ mice spent markedly reduced time seizing during this scoring period compared with controls (Figure 6C) and were completely protected from seizure-induced death (Figure 6D).

These results confirm the importance of caspase-1 in seizure propagation. Yet, the CNS cell type harboring these pathogenic inflammasomes remained unknown. To address this, we generated mice deficient for caspase-1 in defined CNS cell types and assessed relative seizure severity in these animals. We first explored a role for microglial-specific caspase-1 deletion in our model, as microglia have been most frequently implicated in inflammasome-driven neurological diseases. However, we observed no appreciable differences in seizure severity, onset, duration, or survival following caspase-1 deletion in microglia ($Casp1^{fl/fl}$;$Cx3cr1^{Cre}$ or $Casp1^{\Delta MG}$ mice) when compared with Cre-negative $Casp1^{fl/fl}$ littermate controls ($Casp1^{cont}$; Figures S6R–S6U). We then speculated that pathogenic inflammasome activation in a hyperexcitable seizure context could be driven by

neurons themselves. We therefore turned to neuron-specific caspase-1 conditional knockout mice, $Casp1^{fl/fl}$;$Synapsin^{Cre}$ ($Casp1^{\Delta Syn}$) and respective Cre-negative $Casp1^{fl/fl}$ littermate controls ($Casp1^{cont}$). Opposite to full-body caspase-1-deficient mice, which were protected from severe seizures (Figures 6A–6D), we found that mice lacking caspase-1 specifically in neurons were slightly more susceptible to KA-induced seizures (Figures S6V–S6Y). These collective findings reveal that caspase-1 likely does not act in microglia or neurons to propagate seizures in our model.

Astrocytes are vitally important in neurotransmitter reuptake and recycling and also play key roles in buffering ion concentrations around synapses,[78,79] placing astrocytes in an optimal position to regulate neuronal hyperexcitability. To explore this, we leveraged our $Casp1^{\Delta Ast}$ mice and subjected these animals to KA seizure experiments alongside respective $Casp1^{cont}$ controls. Here, we found that KA-treated $Casp1^{\Delta Ast}$ mice had significantly lower seizure scores, took longer to begin seizing, and spent less time seizing compared with controls (Figures 6E–6G). Moreover, seizures were less lethal to $Casp1^{\Delta Ast}$ mice than $Casp1^{cont}$ littermate controls (Figure 6H). Taken together, our studies demonstrate that astrocyte-specific inflammasome activation can contribute to seizure propagation. These findings are in line with our homeostatic studies showing that blockade of caspase-1 signaling in astrocytes reduces physiologic neuronal activity and collectively illustrate the importance of astrocyte-dependent inflammasome signaling in maintaining hippocampal physiology.

DISCUSSION

Findings from these studies identify an unexpected function for inflammasome signaling in regulating astrocyte-neuron communication and underlying hippocampal plasticity. We observed environmentally modulated inflammasome assembly in the homeostatic adult brain and that hippocampal astrocytes harbor ASC specks. Functionally, pharmacologic inhibition of caspase-1 or genetic deletion specifically in astrocytes was sufficient to promote an increase in synaptic protein abundance and to modulate neuron activity. We found that loss of caspase-1 in astrocytes alters plasticity-related gene expression, neurogenesis, PNN coverage, and promoted IL-33 production. Mechanistically, IL-33 from both astrocytes and neurons could modulate many of these plasticity-related effects, and the inflammasome-derived cytokine IL-18 was sufficient to reduce hippocampal IL-33 release. We finally leveraged the ability of caspase-1 to regulate neuronal activity to reduce seizure severity.

While it is well appreciated that aberrant activation of the innate immune system can cause brain pathology and neurological disease progression, there is also an emerging body of literature demonstrating that controlled immune signaling is needed to support healthy brain function. As such, a delicate middle ground of inflammatory signaling in the brain is needed to maintain a balanced homeostatic state. We propose that astrocyte-dependent inflammasome activation acts as a double-edged sword for hippocampal plasticity. On one edge of the sword, the inflammasome appears to curb hippocampal plasticity. The inflammasome and its products (namely, caspase-1, and IL-18) are detrimental to hippocampal neurogenesis, synaptic markers, and IL-33 expression. Modulation of the environment in a way that is positive for hippocampal plasticity correlated with

reduced inflammasome assembly. Given these findings, we were left speculating why the inflammasome is activated at all in the homeostatic hippocampus. We find one answer on the other edge of the sword: that astrocyte caspase-1 is necessary for proper hippocampal activity. We find that blocking inflammasome activity in astrocytes ultimately accelerates forgetting. Our collective results suggest that a balance in inflammasome activity underlies proper hippocampal function.

Blockade of astrocyte inflammasome activation might offer a promising therapeutic strategy to mitigate hippocampal hyperexcitability across several neurologic disease states. We postulate that neuronal activity can act as a switch for inflammasome activity, in which moderate activity turns inflammasome activity down while excessive neuronal activation, which underlies seizures, can instead trigger pathological inflammasome activity. We speculate that the downstream mediators of hippocampal inflammasome activation could also differ depending on the context. Take, for example, the possibility that IL-18 could modulate plasticity-related mechanisms at the steady state, whereas IL-1β or another mediator could instigate pathogenic firing in the context of seizures.

While our studies reveal that astrocyte-dependent inflammasome signaling and IL-18 provide a potential mechanism by which IL-33 release is regulated in the adult brain to modulate hippocampal plasticity, future work is needed to define the full spectrum of ways through which inflammasome signaling can impact astrocyte biology and hippocampal physiology under homeostasis. A single mouse astrocyte can be in contact with several neuronal soma, about 600 dendrites, and around 100,000 synapses.[80] As such, astrocytes are known to control synapse formation, maintenance, and elimination.[81] How the inflammasome fits into this picture of astrocyte-mediated synapse control will remain an area for future investigation.

It will also be important in future studies to delineate the full spectrum of inflammasome sensors that are involved in coordinating hippocampal caspase-1 activation under homeostasis. Given that a large array of inflammasome activators are known to be present in the brain under steady-state conditions (e.g., ATP, extracellular Ca^{2+}, ROS production, K^{+} fluxes, etc.), multiple distinct inflammasome sensors are likely involved in orchestrating hippocampal caspase-1 activation. Moreover, it is feasible that other inflammasome-generated downstream factors such as IL-1 can also independently influence hippocampal physiology.

The findings in this study are notable as they contribute to our knowledge of the mechanisms underlying astrocyte biology and neuronal plasticity. The inflammasome has been a center point of interest as a druggable target for many neurologic disease states, including neurodegenerative disease, epilepsy, stroke, and others.[15] Our work lends to the processes downstream of caspase-1 that might be impacted in these endeavors, including PNN plasticity, synaptic protein abundance, and neuronal activity. Thus, these data may inform therapeutic strategies to treat neurologic diseases associated with perturbed inflammasome activation.

Limitations of the study

We have shown changes to various readouts of hippocampal plasticity following modulation of caspase-1 activity, including that deletion of caspase-1 in adult astrocytes is sufficient to alter intrinsic neuronal firing. Yet, it remains unclear whether the changes in synaptic protein relative abundance following caspase-1 blockade directly contribute to functional changes in synaptic excitatory and/or inhibitory activity. Additional electrophysiological studies should be conducted in the future to assess steady state and evoked synaptic activity in the hippocampus following manipulation of inflammasome components.

We find protection from severe seizures following caspase-1 deletion in an acute KA model. Yet, this is a pre-clinical mouse model with several limitations. Epilepsy constitutes at least two unprovoked seizures that occur more than 24 h apart. Since we did not follow mice after the end of the acute KA-induced seizure, we are limited in this study to extend these findings to reoccurring seizures in the context of epilepsy. The seizures triggered in our KA model are driven by glutamate receptor agonism, which is a simplification of the complex disease states that might trigger seizures, which can include epilepsy, infection, traumatic head injury, stroke, cardiovascular events, or neurodegeneration. Additional studies are needed in other pre-clinical animal models of seizure and epilepsy to more thoroughly assess the downstream impacts of caspase-1 blockade on hippocampal hyperexcitability.

RESOURCE AVAILABILITY

Lead contact

All information and requests for further resources and reagents should be directed to and will be fulfilled by the lead contact, John Lukens (jrl7n@virginia.edu).

Materials availability

All requests for resources and reagents should be directed to and will be fulfilled by the lead contact. This study did not generate new unique reagents.

Data and code availability

All data are available from the lead contact upon request. Raw data from the scRNA-seq study (barcodes, features, and matrix files) are publicly available for download (Mendeley Data: https://data.mendeley.com/datasets/fwtcf2ybbn/1). All code used for bioinformatics analysis is deposited publicly (Zenodo: https://doi.org/10.5281/zenodo.15035203 and GitHub: https://github.com/LukensLab/Casp1Aldh1l1-scRNAseq).

Any additional information required to reanalyze the data reported in this paper is available from the lead contact upon request.

STAR★METHODS

EXPERIMENTAL MODEL AND STUDY PARTICIPANT DETAILS

Mice: All mouse experiments were performed in accordance with the relevant guidelines and regulations of the University of Virginia and approved by the University of Virginia

Animal Care and Use Committee. Mice were housed in specific pathogen-free conditions under standard 12-hr light/dark cycle conditions in rooms equipped with control for temperature (21 ± 1.5°C) and humidity (50 ± 10%). Adult age-matched mice were assigned to experimental groups. Unless age is explicitly noted, mice were assessed beginning at 8-weeks of age. Unless sex is otherwise noted in the figure legend, male and female mice were included for all studies and data was analyzed first separated by sex to check for any significant sex differences before combining. Wild type C57BL/6J (WT; strain #000664), $ASC^{Citrine}$ (strain #030744),[24] $Thy1^{YFP}$ (strain #003782),[85,86] 5xFAD (strain #034848),[87] and $Casp1^{-/-}$ (strain #016621)[88] were obtained from The Jackson Laboratory. TRAP2;tdTomato mice were a generous gift from J. Kipnis which were generated by crossing $Fos^{2A\text{-}iCreERT2}$ (strain #030323)[89,90] with Lox-Stop-Lox-CAG-tdTomato (strain #007914)[91] mice originally from The Jackson Laboratory. $Casp1^{fl/fl}$ were generously provided by R. Flavell[92] and mice were crossed to $Aldh1l1^{Cre\text{-}ERT2}$ (strain #031008)[93] obtained from The Jackson Laboratory to generate $Casp1^{fl/fl}$;$Aldh1l1^{Cre\text{-}ERT2}$ mice (denoted $Casp1^{\Delta Ast}$) and Cre-negative littermate controls (denoted $Casp1^{cont}$). $Casp1^{fl/fl}$ were also crossed to $Synapsin^{Cre}$ mice (strain #003966)[94] obtained from The Jackson Laboratory to generate $Casp1^{fl/fl}$;$Synapsin^{Cre}$ mice (denoted $Casp1^{\Delta Syn}$), or to $Cx3cr1^{Cre}$ mice (strain #025524)[82] obtained from The Jackson Laboratory to generate $Casp1^{fl/fl}$;$Cx3cr1^{Cre}$ mice (denoted $Casp1^{\Delta MG}$) and respective Cre-negative littermate controls (denoted $Casp1^{cont}$). $Il33^{fl/fl}$ were generously provided by R. Sharma and crossed to $Aldh1l1^{Cre\text{-}ERT2}$ mice (strain #031008)[93] obtained from The Jackson Laboratory to generate $Il33^{fl/fl}$;$Aldh1l1^{Cre\text{-}ERT2}$ mice (denoted $Il33^{\Delta Ast}$) or and $Camk2a^{Cre\text{-}ERT2}$ mice (strain #012362)[91] obtained from The Jackson Laboratory to generate $Il33^{fl/fl}$;$Camk2a^{Cre\text{-}ERT2}$ mice (denoted $Il33^{\Delta Neur}$) and respective Cre-negative littermate controls (denoted $Casp1^{cont}$). Upon weaning, $Casp1^{\Delta Ast}$, $Casp1^{cont}$, $Il33^{\Delta Ast}$, $Il33^{\Delta Neur}$, and $Il33^{cont}$ mice were fed tamoxifen diet (Envigo Teklad #TD.130858) *ad libitum* for two weeks and then returned to normal chow for the remainder of experimentation.

Caspase-1 inhibitor treatment: Mice were injected i.p. with the caspase-1 inhibitor VX765 (Apex Bio, A8238) prepared 6.25 mg/ml in 25% DMSO or vehicle (25% DMSO) as a control. 8–12-week old TRAP2;tdTomato ($Fos^{2A\text{-}iCreERT2}$ Lox-Stop-Lox-CAG-tdTomato) mice were injected i.p. with 50 mg/kg VX765 or vehicle control, left to rest for 10 min, and then injected with 150 mg/kg tamoxifen (Millipore Sigma, T5648) in corn oil. After 30 min, mice were placed into an enriched environment for 48 hrs. Mice were then perfused and brains were harvested (see “Tissue collection”). $Thy1^{YFP}$ mice received i.p. injections of 30 mg/kg VX765 or vehicle control 3x/week (Mondays, Wednesdays, and Fridays) beginning two-weeks prior to behavioral testing and continuing for the entirety of experimentation. All mice were always weighed prior to injection.

Environmental enrichment: Mice were brought into a separate room and placed into and enriched environment (EE; rat cages with crushed corn cob bedding) or left in their home cages (11 × 7 × 6 inch mouse cages with crushed corn cob bedding) in the vivarium as a control. $ASC^{Citrine}$, WT, and TRAP2;tdTomato mice were EE housed for 48 hrs or 1 wk under standard 12-hr light/dark cycle conditions in rooms equipped with control for temperature (21 ± 1.5°C) and humidity (50 ± 10%). EE housing conditions consisted of a

mix of colored igloos (Bio-Serv #K3570, #K3327), crawl balls (Bio-Serv #K3329, #K3330), and tunnels (Bio-Serv #K3322, #K3323) with *ad libitum* access to standard chow and water. Mice were euthanized, perfused, and brains harvested immediately following all EE treatments (see "Tissue collection").

Seizure induction: Seizures were induced in 6-week-old WT, Casp1$^{-/-}$, Casp1$^{\Delta Syn}$ (alongside Casp1^{cont} littermates), and Casp1$^{\Delta MG}$ (alongside Casp1^{cont} littermates) by i.p. injection of 24 mg/kg kainic acid (KA; Tocris, #7065) in 1x PBS. Seizures were induced in 6-week-old Casp1$^{\Delta Ast}$ (alongside Casp1^{cont} littermates) by i.p. injection of 16 mg/kg KA. Seizing mice were scored every 5 min for 2 hrs post injection using a modified Racine scale, as follows: 0 = normal activity, 1 = immobility, 2 = rigid posture and raised tail, 3 = forelimb clonus (seizure onset), 4 = forelimb and hindlimb clonus with rearing and falling, 5 = continuous stage four often with lying down, 6 = intense seizures with jumping (seizure spells), 7 = death. Once a mouse scored a 1 it was never scored back to 0. Once a mouse scored a 4 it was never scored below a 3 again. Once a mouse scored a 7 it was scored at 7 for the remainder of the experiment.

METHOD DETAILS

Behavior analysis: All behavior experiments were performed between 8 am and 5 pm in a blinded fashion. Mice were transported from their home vivarium room to the behavior core and allowed 20 minutes to habituate before beginning each test. All training apparatuses were cleaned with 70% ethanol before and after each mouse was tested.

Morris water maze: Spatial learning and memory were engaged using the Morris water maze. A white plastic pool (1 m in diameter) contained water kept at 22 ± 2°C and made opaque with non-toxic white tempura paint. A hidden platform (10 cm in diameter) was placed 1 cm below the water surface. Four distinct visual cues within each quadrant were placed equally spaced around the walls of the pool. A dim light source evenly illuminated the test room.

The training phase of this task consisted of four 60 s trials per day for four days, and the probe trial consisted of a single 60 s trial in which the hidden platform was removed from the pool. If the mouse was unable to locate the platform within the trial time allotted, then it was manually placed onto the platform. Mice were allowed 2 min to sit on the platform following the very first training trial, and 5 s to sit on the platform for every trial afterwards. Mice were removed from the pool, dried, and returned to their home cages set upon heating pads between each trial on training days. At least 30 min was given between each training trial. All trials were tracked and scored using an overhead camera and video monitoring software (Ethovision XT Noldus).

ASC^{Citrine} mice were harvested immediately following the fourth trial on training day 2 or immediately following the probe trial on day 5 (see "Tissue collection"). Control ASC^{Citrine} mice for these experiments underwent identical testing procedures except without any hidden platform within the pool during the entire training phase. Swim-only control mice were harvested immediately following the probe trial on day 5.

Rotarod: Gross motor function and motor learning were engaged on the rotarod. The rotarod apparatus consists of five separate compartments on a rotating rod (MED Associates Inc, ENV-575M). Each mouse was placed onto the rod at a speed of 4 rpm. The rod accelerated from 4 rpm to 40 rpm over the span of 5 min. Each mouse was allowed to walk on the rotating rod until one of the three trial endpoints was reached: falling off to disrupt a laser at the base, 5 rotations hanging on the rod without ambulating, or elapsing 6 min of testing. Three trials were performed with at least 30 min between each trial for three consecutive days. $ASC^{Citrine}$ mice underwent an additional memory probe trial four days later (day 7) in which mice were made to run on the rotarod for 6 min total. Mice that fell off were placed back on the rotating rod continually after successive falls until 6 min had elapsed from the start of the recall trial. $Casp1^{\Delta Ast}$ and $Casp1^{cont}$ mice did not undergo this memory recall probe trial. Latency to fall and rotarod speed at fall were recorded by the rotarod-controlling software (rotarod version 1.4.1, MED Associates Inc).

For the rotarod task using $ASC^{Citrine}$ mice, animals were harvested immediately following the first trial on training day 1 (“Activation” group), immediately following the third trial on day 2 (“Learn” group), or immediately following a single memory probe trial on day 7 (“Recall” group; see “Tissue collection”). Control $ASC^{Citrine}$ mice for these experiments (“Home” group) were not brought into the testing room and were harvested immediately from their home cages upon removal from the vivarium. $Casp1^{\Delta Ast}$ and $Casp1^{cont}$ mice were harvested at the end of all behavioral testing.

Open field: General locomotion, exploratory, and anxiety-related behaviors were assessed using the open field test. The opaque white Plexiglass test arenas (35×35 cm^2) were evenly illuminated. Mice were placed into the center of the arena and allowed to explore for 10 min. All trials were tracked and scored using an overhead camera and video monitoring software (Ethovision XT Noldus). A central square (20×20 cm^2) was demarcated to quantify time spent in the center.

Elevated plus maze: Exploratory and anxiety-related behaviors were assessed using the elevated plus maze. The maze consisted of two open arms (uncovered, 35×6 cm^2) and two closed arms (20 cm tall opaque black Plexiglass, 35×6 cm^2) extending from a common center square, elevated 121 cm above the floor. Mice were placed onto the opaque white Plexiglass floor in the center facing a closed arm, and then allowed to explore the entire raised platform for 5 min. All trials were tracked and scored using an overhead camera and video monitoring software (Ethovision XT Noldus).

Fear conditioning memory persistence testing: Spatial memory retention was assessed using a fear conditioning paradigm. The training chamber (MED Associates Inc) consisted of an arena ($28 \times 21 \times 22$ cm) with clear plexiglass walls and a floor made of 18 stainless steel rods (4 mm in diameter) spaced 1.5 cm apart and wired to a shock generator. The chamber was kept inside a sound-proof box which was evenly lit with a white, fluorescent light and supplied with background noise.

For fear conditioning training, mice were placed into the center of the arena and allowed to habituate for 3 min. Mice then received three pairs of cue-aversive stimuli over 3 min

consisting of tone (18 s, 5 kHz, 75 dB) with shock (2 s, 5 mA) pairings separated by 40 s inter-trial-intervals. Mice were assessed in a context test on subsequent testing days (24 hr, 3 wk, 7 wk, and 11 wk). During these contextual fear conditioning tests, mice were placed into the center of the arena as it appeared during the training session and allowed to explore freely for 3 min. No tone or shock were presented during these sessions.

Mice were kept in their home cages in the vivarium without any additional behavioral interventions during the entirety of this 11 wk testing period. After the final 11 wk context test, mice were exposed to a novel environment in which the arena was altered in appearance such that black-and-white striped paper was placed over the walls, a white plastic insert covered the floor, and the chamber was scented with vanilla. Mice were placed into the center of this arena and allowed to explore this novel context for 3 min. Percent freezing in this novel environment was quantified to compare to trained context-specific freezing.

All trials were tracked and scored using an overhead camera and video monitoring software (Ethovision XT Noldus). Percent freezing was calculated as the cumulative time immobile divided by the total test time (180 s), multiplied by 100. The discrimination index was calculated as (A−B)/(A+B), where A = [% freezing in the trained context] and B = [% freezing in the novel context], where 1 indicates full relative immobility in the familiar context and −1 indicates full relative immobility in the novel context.

Tissue collection: Mice were euthanized by CO_2 asphyxiation and cervical dislocation, then transcardially perfused with 20 ml ice cold 1x PBS and brains were harvested. For all experiments involving immunohistochemistry, western blotting, ELISA, and qPCR, brains were cut down the midline, and the right hemisphere was optionally microdissected to remove the hippocampus which were flash-frozen on dry ice. Microdissected samples and half-brain right hemispheres were stored at −80°C until downstream processing for protein or RNA extraction. The left hemisphere was kept intact for downstream immunohistochemistry and drop-fixed in 4% PFA on ice, then stored overnight at 4°C. The following day, PFA was decanted, brains were washed in 1x PBS, and then 10 ml of 30% sucrose was added. Brains were kept in 30% sucrose at 4°C until sinking to the bottom of the container (at least 48 hrs) at which point they were prepped for cryosectioning (see “Brain sample preparation”).

Brain sample preparation: Drop-fixed half-brains sufficiently dehydrated in 30% sucrose (see “Tissue collection”) were washed with 1x PBS and frozen in Tissue-Tek OCT compound (Sakura #4583). Frozen blocks were sectioned at 40 μm using a cryostat (Leica) and sections were stored in 0.05% sodium azide in 1x PBS at 4°C for downstream immunohistochemistry (see “Immunofluorescence”). Flash-frozen half-brains or microdissected brain regions were minimally thawed on ice and mechanically homogenized in Tissue Protein Extraction Reagent (T-PER; Thermo Fisher, 78510) containing phosphatase inhibitor cocktail PhosSTOP (Roche, 04906845001) and protease inhibitor cocktail cOmplete (Roche, 11873580001). Half-brains or half-hippocampi were homogenized in 500 μl or 200 μl of this TPER cocktail, respectively. 50 μl of these slurries were then added to Trizol (500 μl for half-brains or 250 μl for half-hippocampi; Life Technologies, 15596018) and stored at −80°C until further use (see “RNA isolation, cDNA

synthesis, qPCR"). The remainder of the slurries were then spun down at 16,000 rpm for 10 minutes and the soluble supernatants were collected and stored at −80°C until further use (see "Western blotting" and "ELISA").

Fluorescence tracking in primary CNS cells: Fresh brains were isolated from adult $ASC^{Citrine}$ mice and were briefly placed in HBSS +Ca +Mg on ice before being transferred into 5 ml enzymatic buffer (HBSS +Ca +Mg supplemented with 4 U/ml papain (Worthington Biochemical, LS003127) and 50 U/ml DNase I (Roche, 10104159001)) at room temperature. Samples were triturated with a 5 ml pipette and incubated for 15 min at 37°C. Samples were triturated with a 1 ml pipette and then returned for 37°C for another 15 min incubation. This was repeated once more, for a total of 45 min at 37°C and 3 trituration steps. The resulting single cell suspension was passed through a 70 μm cell strainer followed by 20 ml dissociation buffer (DMEM/F12 supplemented with 10% FBS, 0.1% GlutaMAX, and 0.1% antibiotic-antimycotic). Cells were spun down at 1500 rpm for 5 min at 4°C, washed in 1x PBS, and then spun down again at 1500 rpm for 5 min at 4°C. The resulting cell pellet was resuspended in 1 ml 37% isotonic Percoll (Cytiva, 17–0891-02) and then 12 ml 37% isotonic Percoll was added. Samples were spun down on this Percoll gradient at 2000 rpm for 12 min with no brake at room temperature. The myelin debris and remaining supernatants were aspirated, and the final cell pellet was resuspended in enough FACS buffer (1x PBS with 0.2% 1 M EDTA and 0.2% BSA) to plate 12 wells per mouse brain (ex. 2.4 ml total for 200 μl per well). Cells were spun down at 1500 rpm for 5 min at 4°C in a flat bottom plate and then baseline $ASC^{Citrine}$ fluorescence was read on a BioTek Cytation 5 Cell Imaging Multimode Reader (Aligent). Treatment conditions (no treatment, 2 mM $CaCl_2$ (BioVision, B1010–100), or 100 μM etoposide (Millipore Sigma, E1383)) in FACS buffer were added to the wells and fluorescence was read every hour for 6 hrs. Cells were then spun down at 1500 rpm for 5 min at 4°C, the plate was flicked to remove buffer, and then fresh FACS buffer was added overnight. Fluorescence was read again in the morning (18 hrs post-treatment) after overnight washout.

Hippocampus isolation and *ex vivo* treatments: Brains were isolated from adult mice and hippocampi were immediately microdissected, cut in half sagittally, and then held in warm plating media (Neurobasal-A media (Thermo Fisher, 10888022), 2% B27 (Thermo Fisher, 17504044), 0.1% GlutaMAX (Thermo Fisher, 35050061), 0.1% antibiotic-antimycotic (Thermo Fisher, 15240096)). Treatment conditions (no treatment, NT; 30 or 60 μM forskolin (FSK; Tocris, 1099); 50, 100, or 1000 μM glutamate (prepared from L-glutamic acid (Millipore Sigma, G1251) with 1 M HCl (Fisher Scientific, A144–212); 1, 100, or 500 ng/ml IL-18 (Fisher Scientific, #KMC0181)) in plating media were added to the wells. Samples were incubated at 37°C for 30 min or 2 hrs, and then supernatants were collected and hippocampi were flash frozen all for storage at −80°C.

Electrophysiology recordings: Preparation of acute brain slices for electrophysiology experiments was modified from standard protocols previously described.[95–97] Eight-to-twelve-week-old $Casp1^{\Delta Ast}$ and $Casp1^{cont}$ mice were anesthetized with isoflurane and decapitated. The brains were rapidly removed and kept in chilled artificial cerebrospinal fluid (ACSF) at 4°C containing (in mM): 125 NaCl, 2.5 KCl, 1.25 NaH_2PO_4, 2 $CaCl_2$, 1

$MgCl_2$, 0.5 L-ascorbic acid, 10 glucose, 25 $NaHCO_3$, and 2 Na-pyruvate (osmolarity 310 mOsm). Slices were continuously oxygenated with 95% O_2 and 5% CO_2 throughout the preparation. Coronal brain sections at 300 μm were prepared using a Leica Microsystems VT1200 vibratome. Slices were collected and placed in ACSF warmed to 37°C for 30 minutes and then kept at room temperature for up to 5 hours.

Patch-clamp recordings: Brain slices were placed in a chamber superfused (~2 ml/min) with continuously oxygenated recording solution warmed to 32 ± 1°C. Pyramidal CA1 neurons were identified by video microscopy based on hippocampus morphology. Whole-cell electrophysiology recordings were performed using a Multiclamp 700B amplifier with signals digitized by a Digidata 1550B digitizer. Currents were amplified, lowpass-filtered at 2 kHz, and sampled at 35 kHz. Borosilicate electrodes were fabricated using a Brown-Flaming puller (model P1000, Sutter Instruments) to have pipette resistances between 2.5 and 4.5 mΩ. Current-clamp recordings of neuronal excitability were collected in ACSF solution identical to that used for preparation of brain slices. The internal solution contained the following (in mM): 120 K-gluconate, 10 NaCl, 2 $MgCl_2$, 0.5 K2 EGTA, 10 HEPES, 4 ATP-Na_2, and 0.3 GTP-Na, pH 7.2 (osmolarity 290 mOsm). Intrinsic excitability was assessed using methods adapted from those previously described.[90,91] Briefly, resting membrane potential was manually recorded from the neuron at rest. Current ramps from 0 to 400 pA over 4 seconds were used to calculate passive membrane and action potential (AP) properties, including threshold, upstroke and downstroke velocity, which are the maximum and minimum slopes on the AP, respectively; amplitude, which was defined as the voltage range between AP peak and threshold; APD_{50}, which is the duration of the AP at the midpoint between threshold and peak. AP frequency–current relationships were determined using 1-second current injections from −40 to 600 pA. Spikes were only counted if AP overshoot was >0 mV and amplitude was >20 mV. Input resistance was calculated from the −20 pA pulse. Analysis of electrophysiological data was performed in a blinded manner.

Magnetic-activated cell sorting: For isolation of astrocytes alone from $Casp1^{\Delta Ast}$ and $Casp1^{cont}$ mice, fresh whole brains held in HBSS on ice were dissociated using a Papain Dissociation System (Worthington, LK003150) according to manufacturer's instructions with some modifications. Briefly, tissue was transferred into the Papain Solution (EBSS with 20 U/ml papain and 0.005% DNAse) and triturated gently using a 5 ml serologic pipette. The mixture was incubated at 37°C on a shaker for 30 min in which it was triturated gently every 10 min (3x). The cloudy cell solution was then filtered through a 70 μm cell strainer and spun down at room temperature at 300 g for 5 min. The resulting cell pellet was resuspended in the Inhibitor Solution (EBSS with papain/ovomucoid inhibitor solution and DNAse). This cell solution was then layered atop fresh Inhibitor Solution and centrifuged at 70 g for 6 min at room temperature. The supernatant containing debris was discarded, and the remaining cell pellet was resuspended in 160 μl 1x MACS buffer (Miltenyi Biotec, 130–0910376) in 1x PBS.

Astrocytes were positively selected using ACSA2 magnetic microbeads (Miltenyi Biotec, 130–097-678) according to manufacturer's instructions with some modifications. Briefly, the cell suspension was incubated with 40 μl FcR-blocking reagent for 25 min at 4°C. Then,

40 µl anti-ACSA2 magnetic microbeads were added, mixed well, and allowed to incubate for 15 min at 4°C. Cells were washed by adding 1 ml 1x MACS buffer and centrifuged at 300 g for 10 min at 4°C. Supernatants were aspirated and the remaining cell pellet was resuspended in 500 µl 1x MACS buffer. LS columns (Miltenyi Biotec, 130–042-401) and a QuadroMACS magnet (Miltenyi Biotec, 130–091-051) were used to positively select for ACSA2+ cells. Positive and negative fractions were spun down at 300 g for 10 min at 4°C. ACSA2+ and ACSA− pellets were then resuspended in 200 µl or 500 µl Trizol reagent, respectively, for downstream RNA extraction (see "RNA isolation, cDNA synthesis, qPCR").

For isolation of neurons and astrocytes together from $Casp1^{\Delta Ast}$ and $Casp1^{cont}$ mice, fresh whole brains held in HBSS on ice were dissociated using a neural tissue dissociation kit (Miltenyi, 130–094-802) according to manufacturer's instructions. Briefly, brains were washed in 1x PBS and then placed in 6 ml 1x PBS. Brains were triturated gently using a 5 ml serologic pipette, tissue was allowed to settle, and then the supernatant was carefully removed. 1960 µl enzyme mix 1 was added and then samples were incubated for 15 min at 37°C on a shaker. 30 µl enzyme mix 2 was added and then tissue was dissociated carefully using a 1 mL pipette. Samples were incubated for 10 min at 37°C on a shaker and then 15 µl enzyme mix 2 was added. Tissue was again dissociated carefully using a 1 ml pipette. The cloudy cell solution was then filtered through a 70 µm cell strainer followed immediately by 10 ml 0.5% BSA in 1x PBS. Samples were spun down at room temperature at 300 g for 5 min. Supernatants were carefully aspirated and the cell pellets were resuspended in 160 µl 1x MACS buffer.

Neurons were negatively selected using an adult neuron isolation kit (Miltenyi, 130–126-603) according to manufacturer's directions. Briefly, the cell suspension was incubated with 40 µl adult non-neuronal cell biotin antibody cocktail for 5 min at 4°C. Cells were washed in 1 ml 1x MACS buffer and then spun down for 10 min at 4°C. Cells were resuspended in 160 µl 1x MACS buffer and then incubated with 40 µl anti-biotin microbeads for 10 min at 4°C. 500 µl 1x MACS buffer was added and then samples were immediately subject to magnetic separation. LS columns and a QuadroMACS magnet were used to negatively select for neuronal cells. Positive and negative fractions were spun down at 300 g for 10 min at 4°C, washed once with 1 ml 1x MACS buffer, and then spun at 300 g for 10 min at 4°C. The positive fraction (non-neuronal cells) was resuspended in 160 µl 1x MACS buffer and the negative fraction was resuspended in 200 µl Trizol reagent and stored at −80°C. The positive (non-neuronal) fraction was then subject to astrocyte sorting using ACSA2 magnetic microbeads exactly as previously described. Positive and negative fractions were spun down at 300 g for 10 min at 4°C. ACSA2+ and ACSA2− pellets were then resuspended in 200 µl Trizol reagent and stored at −80°C for downstream RNA extraction (see "RNA isolation, cDNA synthesis, qPCR").

Immunofluorescence: Brain sections stored in PBS with 0.05% sodium azide were blocked for 1 hr at room temperature in blocking solution (2% donkey serum, 1% BSA, 0.1% Triton-X, 0.05% Tween-20 in 1x PBS). Sections were then incubated with primary antibodies diluted in the blocking solution overnight at 4°C. The following antibodies were used: Aldh1l1 (E7I2Q, Cell Signaling, 1:500), ASC (AL177, AdiopoGen,

1:300), Calbindin (D-28K, Millipore Sigma, 1:1000), CD68 (FA-11, BioRad, 1:1000), cFos (ab190289, Abcam, 1:1000), GFAP (2.2B10, Thermo Fisher, 1:1000), GSDMD (ab209845, Abcam, 1:1000), Homer-1 (160 003, Synaptic Systems, 1:500), IBA1 (ab5076, Abcam, 1:300), IL-33 (AF3626, R&D, 1:100), Ki67 (606–5698-82, ThermoFisher, 1:100), MAP2 (M13 #13–1500, Thermo Fisher, 1:500), NeuN (MAB377, Millipore Sigma, 1:500), P2RY12 (AS-55043A, AnaSpec, 1:300), S100β (15146–1-AP, Proteintech, 1:500), SOX9 (EPR14335–78, Abcam, 1:500), Synapsin1/2 (106 004, Synaptic Systems, 1:1000), Synaptophysin (ab32594, Abcam, 1:1000), Synaptophysin (ab16659, Abcam, 1:300), VGLUT1 (135 511, Synaptic Systems, 1:500), and WFA (B-1355–2, Vector Laboratories, 1:500). Samples were washed for 10 min three times with 0.5% Tween-20 in 1x PBS at room temperature. Then, samples were incubated with secondary antibodies diluted in the blocking solution for 2 hrs at room temperature. Matched donkey Alexa Fluor-488, −568, −594, −647 anti-rabbit, -goat, -mouse, -rat, and -streptavidin antibodies were used (Thermo Fisher, 1:1000). Samples were washed again for 10 min three times with 0.5% Tween-20 in 1x PBS at room temperature and then incubated with DAPI (Millipore Sigma, 1:1000) in 1x PBS for 10 min at room temperature.

For sections stained with NeuroTrace, secondary antibody staining was completed as well as final wash steps. Then, sections were washed once with 0.1% Triton-X in 1x PBS for 10 min and then twice in 1x PBS for 5 min all at room temperature. Sections were incubated with NeuroTrace 500/525 (N21480, Thermo Scientific, 1:100) diluted in 1x PBS for 20 min at room temperature. Sections were removed from this stain and then washed once with 0.1% Triton-X in 1x PBS for 10 min and then once in 1x PBS for 2 hr at room temperature. Following this last wash step, DAPI counterstaining was conducted as usual prior to section mounting.

For sections stained by TUNEL, secondary antibody staining was completed as well as final wash steps prior to staining according to the manufacturer's protocol (Millipore Sigma, 11684795910). Briefly, sections were washed twice with 1x PBS at room temperature and then incubated with 100 μl TUNEL reaction mixture for 60 min at 37°C on a shaker in the dark. Sections were then washed three times with 1x PBS at room temperature. Following this last wash step, DAPI counterstaining was conducted as usual prior to section mounting.

For sections stained with PI, secondary antibody staining was completed as well as final wash steps prior to staining according to the manufacturer's protocol (Thermo Fisher, P1304MP). Briefly, sections were equilibrated in 2x SSC (Millipore Sigma, S6639) prior to incubation in DNase-free RNase (100 μg/ml in 2x SSC; Roche, 11119915001) for 30 min at 37°C on a shaker in the dark. Sections were then washed three times for 1 min in 2x SSC at room temperature. Sections were equilibrated in 2x SSC prior to staining with PI (10 μg/ml in 2x SSC) for 10 min at room temperature. Sections were finally washed twice in 2x SSC at room temperature. Following this last wash step, DAPI counterstaining was conducted as usual prior to section mounting.

All staining and washing steps were always performed on a rocker. Samples were stored in 1x PBS prior to mounting on slides with ProLong Gold anti-fade mountant (Thermo Fisher, P36930) with coverslips. Slides were stored in the dark at 4°C. Images were acquired using

LAS AF software (Leica microsystems) on a Leica TCS SP8 confocal microscope or Leica Stellaris confocal microscope. Images were analyzed using Fiji and Imaris (9.9.1) software.

Reconstruction of neuronal spines: All hippocampus images were acquired in the CA1 region and all cortex images were acquired in approximately the somatosensory and somatomotor cortices. Thy1^{YFP} expression is selective for layer V pyramidal neurons in the cortex and pyramidal neurons in the CA1, thus, these neuron subtypes were included in the spine density quantifications. Apical segments of the labeled neurons were selected for analysis in the CA1, while no particular segments were selected for in cortical cells. Thus, the spine density calculation is an approximate average across all types of dendrite segments within this region. At least 5 process segments per FOV were analyzed, and all segments in 3 FOVs per mouse per brain region were averaged.

Imaris software (9.9.1) was utilized to create 3D reconstructions of the Thy1^{YFP} dendritic segments using the Filaments tool. The following settings were used for all reconstructions: Autopath (no loops) algorithm, Diameter Calculate = true, Dendrite Starting Point Diameter = Manually set by experimenter, Dendrite Seed Point Diameter = Manually set by experimenter, Dendrite Starting Point Threshold Low = Automatic, Dendrite Starting Point Threshold High = Automatic, Dendrite Seed Point Threshold = Automatic, Diameter around Starting Point(s) to remove Seed Points = Manually set by experimenter, Remove Disconnected Segments = false, Remove Disconnected Segments Smooth Width = Manually set by experimenter, Remove Disconnected Segments Background Subtraction = false, Dendrite Diameter Threshold = Automatic, Dendrite Diameter Algorithm = Distance Map, Spine Seed Point Diameter = 0.400 μm, Spine Maximum Length = 2.00 μm, Spine Allow Branch Spines = false, Spine Seed Point Threshold = Manually set by experimenter, Spine Diameter Threshold = Automatic, Spine Diameter Algorithm = Distance Map.

The experimenter was blind to treatment groups during Filament reconstruction and data analysis. Specific dendrite calculation values were exported to Excel, statistics calculated in R, and data were plotted in Prism.

RNA isolation, cDNA synthesis, qPCR: Brain samples or primary cells stored in TRIzol (see “Brain sample preparation” and “Magnetic activated cell sorting”) were thawed on ice and vortexed. 100 μl of chloroform (Fisher Scientific, BP1145–1) was added, and then samples were thoroughly vortex and incubated at room temperature for 5 min. Samples were spun down at 14,000 rpm at 4°C for 15 min. The clear aqueous top layer was collected into a clean tube and then an equal volume of isopropanol (~400 μl; Sigma, I9516) was added then vortexed vigorously. Samples were then incubated at room temperature for 10 min and spun down at 12,000 rpm at 4°C for 5 min. The resulting RNA pellet was then washed twice using 1 ml of 70% ethanol in RNAse-/DNAse-free water and spun down at 14,000 rpm at 4°C for 5 min between washes. The resulting RNA pellet was air dried at room temperature and finally resuspended in 10–30 μl of DNAse-/RNAse-free water. Samples were stored at −80°C prior to cDNA synthesis. RNA quality and quantity were evaluated using NanoDrop 2000 Spectrophotometer (Thermo Scientific).

Isolated RNA was converted to cDNA using a Sensifast cDNA Synthesis kit (Bioline, BIO-65054). Gene expression levels for all genes (except for *Il33a* and *Il33b*) were determined using Taqman Gene Expression Assay primer/probe mix (Thermo Fisher), Sensifast Probe No-ROX kit (Bioline, BIO-86005), and a CFX384 Real-Time PCR System (BioRad, 1855484). All kits were used according to manufacturer's instructions. The following primers (Thermo Fisher Scientific) were used: *Aim2* (Mm01295720_m1), *Casp1* (Mm00438023_m1; exons 1–3), *Casp1* (Mm01243908_m1; exons 7–9), *Il1b* (Mm00434228_m1), *Gapdh* (Mm99999915_g1), *Il18* (Mm00434226_m1), *Il18r1* (Mm00515178_m1), *Nlrp3* (Mm00840904_m1), *Pycard* (Mm00445747_g1), *Rbfox3* (Mm01248781_m1), and *Slc1a2* (Mm01275814_m1). Relative gene expression levels to *Gapdh* were calculated using the delta-delta Ct method.

For assessing *Il33a* and *Il33b* gene expression levels, custom primers were synthesized from Integrated DNA Technologies for the following sequences: *Il33a*, F: GCTGCAGAAGGGAGAAATCACG; *Il33a*, R: GGAGTTGGAATACTTCATTCTAGGTCTCAT; *Il33b*, F: GGCTCACTGCAGGAAAGTACAGCA; *Il33b*, R: GGAGTTGGAATACTTCATTCTAGGTCTCAT. Reactions were made using Sensifast SYBR No-ROX kit (Meridian Bioscience, BIO-98020) and a CFX384 Real-Time PCR System according to manufacturer's instructions. Relative gene expression levels to *Actin* were calculated using the delta-delta Ct method.

Single cell RNA-sequencing: $Casp1^{cont}$ and $Casp1^{\Delta Ast}$ mice (14-week-old female littermates across two litters) were euthanized by CO_2 asphyxiation and then transcardially perfused with 20 ml ice cold 1x PBS and brains were immediately harvested. The entire hippocampus from the right hemisphere was isolated and placed into 4 ml enzyme solution (master buffer containing 200 U of papain per brain (Worthington Biochemical, LS003127) and 0.5 mM EDTA (Research Products International, E14000–500.0)) on ice. The master buffer contained 1x EBSS (Millipore Sigma, E7510), 0.46% glucose (Millipore Sigma, G8769), and 26 mM $NaHCO_3$ (Millipore Sigma, S6014) in diH_2O. 125 U/ml DNAse I (Roche, 10104159001) was added fresh to the master buffer on the day of procedure. Six total mice were harvested, and three hippocampi per group were pooled to yield two final samples ($Casp1^{cont}$ and $Casp1^{\Delta Ast}$). Pooled hippocampus samples were incubated for 40 min at 37°C in the described enzyme solution with the tissue being agitated every 10 min. Samples were then washed three times with 3 ml 1x low-ovomucoid solution in master buffer (10x low-ovomucoid stock solution contained 15 mg/ml of BSA (Fisher Scientific, BP1600–100) and 15 mg/ml of ovomucoid (Worthington Biochemical, LS003087) adjusted to pH 7.4 using NaOH). Tissue was carefully triturated with a 1 ml pipette and non-homogenized tissue was allowed to settle. Trituration was repeated twice more in this way until most of the tissue became dissociated. Samples were then transferred into clean tubes and 2 ml high-ovomucoid solution in master buffer (10x high-ovomucoid stock solution contained 30 mg/ml of BSA and 30 mg/ml of ovomucoid adjusted to pH 7.4 using NaOH) was carefully pipetted into the bottom of the tube. Samples were spun down at 300 g for 5 min at 4°C and then pellets were resuspended in 5 ml 1x PBS. The cell suspension was passed through a 20 μm Nitex mesh filter, and then spun down at 300 g for 5 min at 4°C.

The resulting pellet was resuspended in 500 μl 1x PBS containing 0.05% BSA and once again spun down at 300 g for 5 min at 4°C.

A dead cell removal cleanup (Miltenyi Biotec, 130–090-101) was then conducted on the single cell suspension according to the manufacturer's protocol. Briefly, samples were resuspended in 100 μl dead cell microbeads and incubated for 15 min at room temperature. LS columns (Miltenyi Biotec, 130–042-401) were washed with 3 ml 1x binding buffer on a magnet stand (MACS MultiStand, Miltenyi Biotec, 130–042-303; fitted with QuadroMACS Separator, Miltenyi Biotec, 130–091-051). 400 μl 1x binding buffer was added to the cell/bead suspension and then applied to the column on the magnet. Columns were washed four times with 3 ml 1x binding buffer. The live cell flow-through was collected and then spun down at 300 g for 5-min at 4°C. The remaining pellet was resuspended in 500 μl 1x PBS containing 0.05% BSA for cell counting. Cells were spun down and finally resuspended in 50 μl 1x PBS containing 0.05% BSA for library preparation.

Library preparation was conducted by the University of Virginia Genome Analysis and Technology core (GATC) as previously reported.[98,99] Briefly, approximately 10,000 cells per sample were processed for library preparation using NGS NSQ2K kit P3 100 cycle v3 and NGS MiSeq kit 300 cycle Nano kits (Illumina) according to validated standard operating procedures established by the GATC (RRID:SCR_018883). The raw sequencing reads (FASTQ files) were aligned to the Genome Research Consortium (GRC) mm10 mouse genome build using Cell Ranger.

R (4.3.2 GUI 1.80 Big Sur ARM build) in RStudio (2023.09.1+494). was used for all downstream analyses. Seurat was used for filtering out low-quality cells, normalization of the data, tSNE clustering, determination of cluster defining markers, and in preparation of some plots. Low-quality cells were excluded in an initial quality control (QC) step by removing cells with low reads (nUMI >= 400), cells with low genes per cell (nGene >= 350), and cells expressing more than 5,000 unique genes (nGene <= 5000) in effort to remove doublets and triplets. Cells with transcriptomes that were more than 10% mitochondrial-derived (mitoratio < 0.1) were removed and cells with low complexity (log10GenesPerUMI > 0.80) were also removed. After these QC and filtered steps, 10,444 $Casp1^{cont}$ cells and 17,864 $Casp1^{\Delta Ast}$ cells remained for all downstream analyses. Cell populations were manually assigned using published literature of population-enriched markers. Differential gene expression analysis was performed for all cells and within each cell cluster using the ZINB-WaVE (v1.24.0) and DESeq2 (v1.42.0) packages. Significantly downregulated and upregulated genes were assayed using GProfiler (https://biit.cs.ut.ee/gprofiler/gost) to generate GO terms. Analyses were performed and plots were generated in RStudio using the following packages: BiocManager, Seurat, dplyr, tidyverse, ggplot2, Matrix, scales, cowplot, RCurl, ggridges, magrittr, patchwork, ggraph, clustree, metap, limma, DESeq2, EnhancedVolcano, RColorBrewer, sctransform, openxlsx, zinbwave, scran.

Western blotting: Soluble brain sample homogenates (see "Brain sample preparation") were diluted in 1x PBS. Protein concentration was determined according to a standard curve using Pierce 600 nm Protein Assay Reagent (Thermo Fisher, 22–660). Laemelli Sample Buffer (Bio-Rad, #1610747) was added at 1x to 20, 40 or 100 μg protein lysates per

sample and heated to 95°C for 5 min. Samples were loaded onto a 4–20% Mini-PROTEAN TGX Stain-Free Protein Gel (Bio-Rad, #4568093) and run at 120 V for 1 hr using Mini-PROTEAN Tetra Cell (Bio-Rad, 1658004) in 1x Tris/Glycine/SDS Buffer (Bio-Rad, #1610732). Proteins were then transferred onto a Trans-Blot Turbo Midi 0.2 μm PVDF membrane (Bio-Rad, #1704157) for 21 min using a Trans-Blot Turbo Transfer System (Bio-Rad, #1704150) set to “2 mini gels” of “mixed MW”.

Membranes were blocked for 1 hr at room temperature using blocking solution (50% SuperBlock T20 TBS Blocking buffer (Thermo Scientific, #37536), 50% BSA block (5% BSA + 0.05% Tween-20 in 1x TBS)). Membranes were then stained overnight at 4°C in primary antibodies diluted in blocking solution. The following antibodies were used: AIM2 (12948S, Cell Signaling, 1:500), ASC (AG25B0006C100, AdipoGen, 1:500), caspase-1 (AG-20B-0042-C100, AdipoGen, 1:500), β-Tubulin (9F3 #5346, Cell Signaling, 1:1000), $GABA_AR\alpha1$ (N95/35, Antibodies Inc, 1:500), GSDMD (126–138, Millipore Sigma, 1:500), IκBα (9242L, Cell Signaling, 1:500), IL-1β (12507S, Cell Signaling, 1:500), IL-18 (54943S, Cell Signaling, 1:500), P-NFκB (3033S, Cell Signaling, 1:500), P-IκBα (2859L, Cell Signaling, 1:500), NFκB (8242S, Cell Signaling, 1:500), NLRP1 (12256–1-AP, Proteintech, 1:500), NLRP2 (15182–1-AP, Proteintech, 1:500), NLRP3 (15101S, Cell Signaling, 1:500), Synaptophysin (ab32594, Abcam, 1;1000), and VGLUT1 (135 511, Synaptic Systems, 1:500). Membranes were then washed for 5 min four times with 1x TBS-T (0.05% Tween-20 in 1x TBS), and then incubated with secondary antibodies diluted in blocking solution for 45 min at room temperature. Matched anti-rabbit (Cell Signaling, 7074P2, 1:5000) or anti-mouse (Cell Signaling, 7076S, 1:5000) HRP secondary antibodies were used. Membranes were then washed for four times with 1x TBS-T over the course of 1–2 hrs. Membranes were coated in SuperSignal West Pico PLUS Chemiluminescent Substrate solution prepared according to manufacturer’s instructions (Thermo Scientific, #34580) for 5 min in the dark prior to imaging. Stained membranes were imaged on a ChemiDoc MP Imaging System (Bio-Rad, #12003154). Protein levels were quantified using Fiji. Membranes were stored in 1x TBS-T at 4°C.

For re-blotting, stained membranes were stripped for 10 min at room temperature using Restore PLUS Western Blot Stripping Buffer (Thermo Fisher, #46430). Membranes were then washed with 1x TBS and then blocked for 1 hr at room temperature using blocking solution. The staining procedure followed from this step.

ELISA: IL-18 protein concentrations in homogenized hippocampus, cerebellum, and cortex samples were determined using an IL-18 ELISA kit (Thermo Fisher, BMS618–3). IL-33 protein concentrations in homogenized hippocampus samples or supernatants were determined using an IL-33 ELISA kit (Thermo Fisher, BMS6025). Frozen microdissected brain regions were thawed on ice and then mechanically homogenized in TPER cocktail (Tissue Protein Extraction Reagent T-PER (Thermo Fisher, 78510) containing phosphatase inhibitor cocktail PhosSTOP (Roche, 04906845001) and protease inhibitor cocktail cOmplete (Roche, 11873580001); 200 μl for hippocampus samples or 500 μl for cerebellum and cortex samples). Slurries were then spun down at 16,000 rpm for 10 min and the soluble supernatants were collected. Protein concentration was determined according to a standard curve using Pierce 600 nm Protein Assay Reagent (Thermo Fisher, 22–660). IL-18 or IL-33

ELISAs were conducted on 50 μl undiluted hippocampal soluble extracts or 50 μl undiluted media supernatants according to the manufacturer's instructions. The plate was read on an Epoch microplate spectrophotometer (Agilent) at 405 nm. IL-18 levels were normalized to total protein loaded.

QUANTIFICATION AND STATISTICAL ANALYSIS

Statistics: Sample sizes were chosen on the basis of standard power calculations (with $\alpha = 0.05$ and power of 0.8). Statistical tests for RNA-seq analyses were conducted using R (4.3.2 GUI 1.80 Big Sur ARM build) in RStudio (2023.09.1+494). All patch-clamp electrophysiology data were analyzed using custom MATLAB scripts or ClampFit 11.2. For electrophysiology data, all statistical comparisons were made using the appropriate test in Prism (GraphPad, 9.5.0). Membrane, action potential properties, and amplitude data underwent descriptive statistics followed by normality and lognormality test using gaussian distribution. Data were assessed form normality using the D'Agostino-Pearson omnibus normality test, Anderson-Darling test, Shapiro-Wilk test, and Kolmogorov-Smirnov test with Dallal-Wilkinson-Lillie for P values. Data were tested for outliers using the ROUT method, and statistical outliers were not included in data analysis. Initial testing was followed by Tukey's test when the gaussian distribution was parametric using a t-test with Welch's correction, and a Kolmogorov-Smirnov test to compare cumulative distributions when nonparametric. For immunofluorescence data, all statistical comparisons were made using linear mixed effects modeling using R (4.3.2 GUI 1.80 Big Sur ARM build) in RStudio (2023.09.1+494). The immunofluorescence data have a nested structure in which 3–9 images were taken per mouse; therefore, the data were analyzed using a linear mixed effects model that can take into account the number of images as well as the number of mice for each measure. This method avoided pseudoreplication (in the case of using only the image datapoints) as well as loss of precision and variability (in the case of only using mouse average values). For all other analyses, Prism software (GraphPad, 10.1.0) was used to calculate mean and S.E.M. values and to conduct statistical significance testing. The following tests were used: unpaired Student's t test, multiple unpaired Student's t tests, one-sample t test with Wilcoxon test against zero, mixed effects analysis, mixed effects analysis with Šídák's multiple comparisons test, mixed effects analysis with uncorrected Fisher's least significant difference test, one-way ANOVA with Tukey's multiple comparisons test, two-way ANOVA, two-way ANOVA with Šídák's multiple comparisons test, and Gehan-Breslow-Wilcoxon test. P values less than 0.05 were considered significant. *P < 0.05, **P < 0.01, ***P < 0.001, ****P < 0.0001, ns = not significant.

Supplementary Material

Refer to Web version on PubMed Central for supplementary material.

ACKNOWLEDGMENTS

We thank members of the Lukens lab and the Center for Brain Immunology and Glia (BIG) at the University of Virginia for valuable discussions. This work was supported by the National Institutes of Health – National Institute of Aging (R01AG071996, R01AG087406, and 1RF1AG078684; awarded to J.R.L.), the Alzheimer's Association (ADSF-21–816651; awarded to J.R.L.), the Cure Alzheimer's Fund (awarded to J.R.L.), The Owens Family Foundation (awarded to J.R.L.), and the Harrison Family Foundation (awarded to J.R.L.). K.E.Z. and H.E. were

supported by Cell and Molecular Biology Training grants (T32GM139787 awarded to K.E.Z. and T32GM008136 awarded to H.E.) and Wagner Fellowships (awarded to K.E.Z. and H.E. separately). A.H. was supported by a Double Hoo Award and a Hutcheson Award. J.D.S. was supported by a University of Virginia Brain Institute Presidential Fellowship and the Immunology Training Program Grant (T32AI007496). M.K.P. and T.C.J.D. were supported by the National Institutes of Neurological Disorders and Stroke (NS122834 and NS120702 awarded to M.K.P.). R.S. and V.S. were supported by the National Institute of Diabetes and Kidney Diseases (R01DK105833; MPI: R.S. and Shu Man Fu) and IGNITE KUH post-doctoral fellowship (I1TL1DK132771, awarded to V.S.). We are grateful to Katriel Cho for the graphical abstract artwork. BioRender.com was used to make figure schemes.

REFERENCES

1. Zengeler KE, and Lukens JR (2021). Innate immunity at the crossroads of healthy brain maturation and neurodevelopmental disorders. Nat. Rev. Immunol. 21, 454–468. 10.1038/s41577-020-00487-7. [PubMed: 33479477]
2. Lenz KM, and Nelson LH (2018). Microglia and beyond: Innate immune cells as regulators of brain development and behavioral function. Front. Immunol. 9, 698. 10.3389/fimmu.2018.00698. [PubMed: 29706957]
3. Colonna M, and Butovsky O (2017). Microglia Function in the Central Nervous System During Health and Neurodegeneration. Annu. Rev. Immunol. 35, 441–468. 10.1146/annurev-immunol-051116-052358. [PubMed: 28226226]
4. Salter MW, and Beggs S (2014). Sublime microglia: Expanding roles for the guardians of the CNS. Cell 158, 15–24. 10.1016/j.cell.2014.06.008. [PubMed: 24995975]
5. Cayrol C, and Girard J-P (2022). Interleukin-33 (IL-33): A critical review of its biology and the mechanisms involved in its release as a potent extracellular cytokine. Cytokine 156, 155891. 10.1016/j.cyto.2022.155891. [PubMed: 35640416]
6. Wang Y, Fu W-Y, Cheung K, Hung K-W, Chen C, Geng H, Yung W-H, Qu JY, Fu AKY, and Ip NY (2021). Astrocyte-secreted IL-33 mediates homeostatic synaptic plasticity in the adult hippocampus. Proc. Natl. Acad. Sci. USA 118, e2020810118. 10.1073/pnas.2020810118. [PubMed: 33443211]
7. Wang Y, Fu AKY, and Ip NY (2021). IL-33/ST2 Signaling Regulates Synaptic Plasticity and Homeostasis in the Adult Hippocampal Circuitry. DNA Cell Biol. 40, 1125–1130. 10.1089/dna.2021.0491. [PubMed: 34297618]
8. Nguyen PT, Dorman LC, Pan S, Vainchtein ID, Han RT, Nakao-Inoue H, Taloma SE, Barron JJ, Molofsky AB, Kheirbek MA, et al. (2020). Microglial Remodeling of the Extracellular Matrix Promotes Synapse Plasticity. Cell 182, 388–403.e15. 10.1016/j.cell.2020.05.050. [PubMed: 32615087]
9. Zheng D, Liwinski T, and Elinav E (2020). Inflammasome activation and regulation: toward a better understanding of complex mechanisms. Cell Discov. 6, 36. 10.1038/s41421-020-0167-x. [PubMed: 32550001]
10. Broz P, and Dixit VM (2016). Inflammasomes: Mechanism of assembly, regulation and signalling. Nat. Rev. Immunol. 16, 407–420. 10.1038/nri.2016.58. [PubMed: 27291964]
11. Sharma D, and Kanneganti T-D (2016). The cell biology of inflammasomes: Mechanisms of inflammasome activation and regulation. J. Cell Biol. 213, 617–629. 10.1083/jcb.201602089. [PubMed: 27325789]
12. Bergsbaken T, Fink SL, and Cookson BT (2009). Pyroptosis: Host cell death and inflammation. Nat. Rev. Microbiol. 7, 99–109. 10.1038/nrmicro2070. [PubMed: 19148178]
13. Yu P, Zhang X, Liu N, Tang L, Peng C, and Chen X (2021). Pyroptosis: mechanisms and diseases. Signal Transduct. Target. Ther. 6, 128. 10.1038/s41392-021-00507-5. [PubMed: 33776057]
14. Walsh JG, Muruve DA, and Power C (2014). Inflammasomes in the CNS. Nat. Rev. Neurosci. 15, 84–97. 10.1038/nrn3638. [PubMed: 24399084]
15. Albornoz EA, Woodruff TM, and Gordon R (2018). Inflammasomes in CNS Diseases. In Inflammasomes: Clinical and Therapeutic Implications Experientia Supplementum, Cordero MD and Alcocer-Gómez E, eds. (Springer International Publishing), pp. 41–60. 10.1007/978-3-319-89390-7_3.

16. Voet S, Srinivasan S, Lamkanfi M, and van Loo G (2019). Inflammasomes in neuroinflammatory and neurodegenerative diseases. EMBO Mol. Med. 11, e10248. 10.15252/emmm.201810248. [PubMed: 31015277]

17. Heneka MT, McManus RM, and Latz E (2018). Inflammasome signalling in brain function and neurodegenerative disease. Nat. Rev. Neurosci. 19, 610–621. 10.1038/s41583-018-0055-7. [PubMed: 30206330]

18. Rijkers K, Majoie HJ, Hoogland G, Kenis G, De Baets M, and Vles JS (2009). The role of interleukin-1 in seizures and epilepsy: A critical review. Exp. Neurol. 216, 258–271. 10.1016/j.expneurol.2008.12.014. [PubMed: 19162013]

19. Mochol M, Taubøll E, Aukrust P, Ueland T, Andreassen OA, and Svalheim S (2020). Interleukin 18 (IL-18) and its binding protein (IL-18BP) are increased in patients with epilepsy suggesting low-grade systemic inflammation. Seizure 80, 221–225. 10.1016/j.seizure.2020.05.018. [PubMed: 32659652]

20. Johnson EA, Guignet MA, Dao TL, Hamilton TA, and Kan RK (2015). Interleukin-18 expression increases in response to neurovascular damage following soman-induced status epilepticus in rats. J. Inflamm. (Lond) 12, 43. 10.1186/s12950-015-0089-9. [PubMed: 26203299]

21. Cumiskey D, Curran BP, Herron CE, and O'Connor JJ (2007). A role for inflammatory mediators in the IL-18 mediated attenuation of LTP in the rat dentate gyrus. Neuropharmacology 52, 1616–1623. 10.1016/j.neuropharm.2007.03.006. [PubMed: 17459425]

22. Cumiskey D, Pickering M, and O'Connor JJ (2007). Interleukin-18 mediated inhibition of LTP in the rat dentate gyrus is attenuated in the presence of mGluR antagonists. Neurosci. Lett. 412, 206–210. 10.1016/j.neulet.2006.11.007. [PubMed: 17123727]

23. Curran B, and O'Connor JJ (2001). The pro-inflammatory cytokine interleukin-18 impairs long-term potentiation and NMDA receptor-mediated transmission in the rat hippocampus in vitro. Neuroscience 108, 83–90. 10.1016/s0306-4522(01)00405-5. [PubMed: 11738133]

24. Tzeng T-CJ, Schattgen S, Monks B, Wang D, Cerny A, Latz E, Fitzgerald K, and Golenbock DT (2016). A fluorescent reporter mouse for inflammasome assembly demonstrates an important role for cell bound and free ASC specks during in vivo infection. Cell Rep. 16, 571–582. 10.1016/j.celrep.2016.06.011. [PubMed: 27346360]

25. Shi J, Zhao Y, Wang K, Shi X, Wang Y, Huang H, Zhuang Y, Cai T, Wang F, and Shao F (2015). Cleavage of GSDMD by inflammatory caspases determines pyroptotic cell death. Nature 526, 660–665. 10.1038/nature15514. [PubMed: 26375003]

26. Liu T, Zhang L, Joo D, and Sun S-C (2017). NF-κB signaling in inflammation. Signal Transduct. Target. Ther. 2, 17023. 10.1038/sigtrans.2017.23. [PubMed: 29158945]

27. Rossol M, Pierer M, Raulien N, Quandt D, Meusch U, Rothe K, Schubert K, Schöneberg T, Schaefer M, Krügel U, et al. (2012). Extracellular Ca2+ is a danger signal activating the NLRP3 inflammasome through G protein-coupled calcium sensing receptors. Nat. Commun. 3, 1329. 10.1038/ncomms2339. [PubMed: 23271661]

28. Kawamoto EM, Vivar C, and Camandola S (2012). Physiology and Pathology of Calcium Signaling in the Brain. Front. Pharmacol. 3, 61. 10.3389/fphar.2012.00061. [PubMed: 22518105]

29. Brini M, Calì T, Ottolini D, and Carafoli E (2014). Neuronal calcium signaling: function and dysfunction. Cell. Mol. Life Sci. 71, 2787–2814. 10.1007/s00018-013-1550-7. [PubMed: 24442513]

30. Semyanov A, Henneberger C, and Agarwal A (2020). Making sense of astrocytic calcium signals — from acquisition to interpretation. Nat. Rev. Neurosci. 21, 551–564. 10.1038/s41583-020-0361-8. [PubMed: 32873937]

31. Thomas RC (2002). The Effects of HCl and CaCl2 Injections on Intracellular Calcium and pH in Voltage-clamped Snail (Helix aspersa) Neurons. J. Gen. Physiol. 120, 567–579. 10.1085/jgp.20028665. [PubMed: 12356857]

32. Lammert CR, Frost EL, Bellinger CE, Bolte AC, McKee CA, Hurt ME, Paysour MJ, Ennerfelt HE, and Lukens JR (2020). AIM2 inflammasome surveillance of DNA damage shapes neurodevelopment. Nature 580, 647–652. 10.1038/s41586-020-2174-3. [PubMed: 32350463]

33. Eckert MJ, and Abraham WC (2013). Effects of Environmental Enrichment Exposure on Synaptic Transmission and Plasticity in the Hippocampus. In Neurogenesis and Neural Plasticity Current Topics in Behavioral Neurosciences, Belzung C and Wigmore P, eds. (Springer), pp. 165–187.
34. Hüttenrauch M, Salinas G, and Wirths O (2016). Effects of Long-Term Environmental Enrichment on Anxiety, Memory, Hippocampal Plasticity and Overall Brain Gene Expression in C57BL6 Mice. Front. Mol. Neurosci. 9, 62. 10.3389/fnmol.2016.00062. [PubMed: 27536216]
35. Jung CKE, and Herms J (2014). Structural Dynamics of Dendritic Spines are Influenced by an Environmental Enrichment: An In Vivo Imaging Study. Cereb. Cortex 24, 377–384. 10.1093/cercor/bhs317. [PubMed: 23081882]
36. Leggio MG, Mandolesi L, Federico F, Spirito F, Ricci B, Gelfo F, and Petrosini L (2005). Environmental enrichment promotes improved spatial abilities and enhanced dendritic growth in the rat. Behav. Brain Res. 163, 78–90. 10.1016/j.bbr.2005.04.009. [PubMed: 15913801]
37. Buschler A, and Manahan-Vaughan D (2012). Brief environmental enrichment elicits metaplasticity of hippocampal synaptic potentiation in vivo. Front. Behav. Neurosci. 6, 85. 10.3389/fnbeh.2012.00085. [PubMed: 23248592]
38. Ohline SM, and Abraham WC (2019). Environmental enrichment effects on synaptic and cellular physiology of hippocampal neurons. Neuropharmacology 145, 3–12. 10.1016/j.neuropharm.2018.04.007. [PubMed: 29634984]
39. Bettio LEB, Rajendran L, and Gil-Mohapel J (2017). The effects of aging in the hippocampus and cognitive decline. Neurosci. Biobehav. Rev. 79, 66–86. 10.1016/j.neubiorev.2017.04.030. [PubMed: 28476525]
40. Driscoll I, Hamilton DA, Petropoulos H, Yeo RA, Brooks WM, Baumgartner RN, and Sutherland RJ (2003). The Aging Hippocampus: Cognitive, Biochemical and Structural Findings. Cereb. Cortex 13, 1344–1351. 10.1093/cercor/bhg081. [PubMed: 14615299]
41. Rao-Ruiz P, Yu J, Kushner SA, and Josselyn SA (2019). Neuronal competition: microcircuit mechanisms define the sparsity of the engram. Curr. Opin. Neurobiol. 54, 163–170. 10.1016/j.conb.2018.10.013. [PubMed: 30423499]
42. Yizhar O, Fenno LE, Prigge M, Schneider F, Davidson TJ, O'Shea DJ, Sohal VS, Goshen I, Finkelstein J, Paz JT, et al. (2011). Neocortical excitation/inhibition balance in information processing and social dysfunction. Nature 477, 171–178. 10.1038/nature10360. [PubMed: 21796121]
43. Adamsky A, Kol A, Kreisel T, Doron A, Ozeri-Engelhard N, Melcer T, Refaeli R, Horn H, Regev L, Groysman M, et al. (2018). Astrocytic Activation Generates De Novo Neuronal Potentiation and Memory Enhancement. Cell 174, 59–71.e14. 10.1016/j.cell.2018.05.002. [PubMed: 29804835]
44. Flores J, Noël A, Foveau B, Beauchet O, and LeBlanc AC (2020). Pre-symptomatic Caspase-1 inhibitor delays cognitive decline in a mouse model of Alzheimer disease and aging. Nat. Commun. 11, 4571. 10.1038/s41467-020-18405-9. [PubMed: 32917871]
45. Flores J, Noël A, Foveau B, Lynham J, Lecrux C, and LeBlanc AC (2018). Caspase-1 inhibition alleviates cognitive impairment and neuropathology in an Alzheimer's disease mouse model. Nat. Commun. 9, 3916. 10.1038/s41467-018-06449-x. [PubMed: 30254377]
46. Magee JC, and Grienberger C (2020). Synaptic Plasticity Forms and Functions. Annu. Rev. Neurosci. 43, 95–117. 10.1146/annurev-neuro-090919-022842. [PubMed: 32075520]
47. Martin SJ, Grimwood PD, and Morris RGM (2000). Synaptic Plasticity and Memory: An Evaluation of the Hypothesis. Annu. Rev. Neurosci. 23, 649–711. 10.1146/annurev.neuro.23.1.649. [PubMed: 10845078]
48. Runge K, Cardoso C, and de Chevigny A (2020). Dendritic Spine Plasticity: Function and Mechanisms. Front. Synaptic Neurosci. 12, 36. 10.3389/fnsyn.2020.00036. [PubMed: 32982715]
49. Martineau M, Guzman RE, Fahlke C, and Klingauf J (2017). VGLUT1 functions as a glutamate/proton exchanger with chloride channel activity in hippocampal glutamatergic synapses. Nat. Commun. 8, 2279. 10.1038/s41467-017-02367-6. [PubMed: 29273736]
50. Ormel L, Stensrud MJ, Bergersen LH, and Gundersen V (2012). VGLUT1 is localized in astrocytic processes in several brain regions. Glia 60, 229–238. 10.1002/glia.21258. [PubMed: 22009457]

51. de Ceglia R, Ledonne A, Litvin DG, Lind BL, Carriero G, Latagliata EC, Bindocci E, Di Castro MA, Savtchouk I, Vitali I, et al. (2023). Specialized astrocytes mediate glutamatergic gliotransmission in the CNS. Nature 622, 120–129. 10.1038/s41586-023-06502-w. [PubMed: 37674083]
52. Rühl S, Shkarina K, Demarco B, Heilig R, Santos JC, and Broz P (2018). ESCRT-dependent membrane repair negatively regulates pyroptosis downstream of GSDMD activation. Science 362, 956–960. 10.1126/science.aar7607. [PubMed: 30467171]
53. Li Y, and Jiang Q (2023). Uncoupled pyroptosis and IL-1β secretion downstream of inflammasome signaling. Front. Immunol. 14, 1128358. 10.3389/fimmu.2023.1128358. [PubMed: 37090724]
54. Evavold CL, Ruan J, Tan Y, Xia S, Wu H, and Kagan JC (2018). The Pore-Forming Protein Gasdermin D Regulates Interleukin-1 Secretion from Living Macrophages. Immunity 48, 35–44.e6. 10.1016/j.immuni.2017.11.013. [PubMed: 29195811]
55. Carty M, Kearney J, Shanahan KA, Hams E, Sugisawa R, Connolly D, Doran CG, Muñoz-Wolf N, Gürtler C, Fitzgerald KA, et al. (2019). Cell Survival and Cytokine Release after Inflammasome Activation Is Regulated by the Toll-IL-1R Protein SARM. Immunity 50, 1412–1424.e6. 10.1016/j.immuni.2019.04.005. [PubMed: 31076360]
56. Lee J-K, Kim S-H, Lewis EC, Azam T, Reznikov LL, and Dinarello CA (2004). Differences in signaling pathways by IL-1β and IL-18. Proc. Natl. Acad. Sci. USA 101, 8815–8820. 10.1073/pnas.0402800101. [PubMed: 15161979]
57. Vukovic J, Borlikova GG, Ruitenberg MJ, Robinson GJ, Sullivan RKP, Walker TL, and Bartlett PF (2013). Immature Doublecortin-Positive Hippocampal Neurons Are Important for Learning But Not for Remembering. J. Neurosci. 33, 6603–6613. 10.1523/JNEUROSCI.3064-12.2013. [PubMed: 23575857]
58. Toda T, Parylak SL, Linker SB, and Gage FH (2019). The role of adult hippocampal neurogenesis in brain health and disease. Mol. Psychiatry 24, 67–87. 10.1038/s41380-018-0036-2. [PubMed: 29679070]
59. Borsini A, Zunszain PA, Thuret S, and Pariante CM (2015). The role of inflammatory cytokines as key modulators of neurogenesis. Trends Neurosci. 38, 145–157. 10.1016/j.tins.2014.12.006. [PubMed: 25579391]
60. Couillard-Despres S, Winner B, Schaubeck S, Aigner R, Vroemen M, Weidner N, Bogdahn U, Winkler J, Kuhn H-G, and Aigner L (2005). Doublecortin expression levels in adult brain reflect neurogenesis. Eur. J. Neurosci. 21, 1–14. 10.1111/j.1460-9568.2004.03813.x. [PubMed: 15654838]
61. Gleeson JG, Lin PT, Flanagan LA, and Walsh CA (1999). Doublecortin is a microtubule-associated protein and is expressed widely by migrating neurons. Neuron 23, 257–271. 10.1016/s0896-6273(00)80778-3. [PubMed: 10399933]
62. Berdugo-Vega G, Arias-Gil G, López-Fernández A, Artegiani B, Wasielewska JM, Lee C-C, Lippert MT, Kempermann G, Takagaki K, and Calegari F (2020). Increasing neurogenesis refines hippocampal activity rejuvenating navigational learning strategies and contextual memory throughout life. Nat. Commun. 11, 135. 10.1038/s41467-019-14026-z. [PubMed: 31919362]
63. Akers KG, Martinez-Canabal A, Restivo L, Yiu AP, De Cristofaro A, Liz Hsiang H-L, Wheeler AL, Guskjolen A, Niibori Y, Shoji H, et al. (2014). Hippocampal Neurogenesis Regulates Forgetting During Adulthood and Infancy. Science 344, 598–602. 10.1126/science.1248903. [PubMed: 24812394]
64. Ikrar T, Guo N, He K, Besnard A, Levinson S, Hill A, Lee H-K, Hen R, Xu X, and Sahay A (2013). Adult neurogenesis modifies excitability of the dentate gyrus. Front. Neural Circuits 7, 204. 10.3389/fncir.2013.00204. [PubMed: 24421758]
65. Luna VM, Anacker C, Burghardt NS, Khandaker H, Andreu V, Millette A, Leary P, Ravenelle R, Jimenez JC, Mastrodonato A, et al. (2019). Adult-born hippocampal neurons bidirectionally modulate entorhinal inputs into the dentate gyrus. Science 364, 578–583. 10.1126/science.aat8789. [PubMed: 31073064]
66. Drew LJ, Kheirbek MA, Luna VM, Denny CA, Cloidt MA, Wu MV, Jain S, Scharfman HE, and Hen R (2016). Activation of local inhibitory circuits in the dentate gyrus by adult-born neurons. Hippocampus 26, 763–778. 10.1002/hipo.22557. [PubMed: 26662922]

67. Dankovich TM, and Rizzoli SO (2022). The Synaptic Extracellular Matrix: Long-Lived, Stable, and Still Remarkably Dynamic. Front. Synaptic Neurosci. 14, 854956. 10.3389/fnsyn.2022.854956. [PubMed: 35350469]
68. Dityatev A, and Schachner M (2003). Extracellular matrix molecules and synaptic plasticity. Nat. Rev. Neurosci. 4, 456–468. 10.1038/nrn1115. [PubMed: 12778118]
69. Jakovljević A, Tucić M, Blažiková M, Korenić A, Missirlis Y, Stamenković V, and Andjus P (2021). Structural and Functional Modulation of Perineuronal Nets: In Search of Important Players with Highlight on Tenascins. Cells 10, 1345. 10.3390/cells10061345. [PubMed: 34072323]
70. Crapser JD, Arreola MA, Tsourmas KI, and Green KN (2021). Microglia as hackers of the matrix: sculpting synapses and the extracellular space. Cell. Mol. Immunol. 18, 2472–2488. 10.1038/s41423-021-00751-3. [PubMed: 34413489]
71. Pérez-Rodríguez DR, Blanco-Luquin I, and Mendioroz M (2021). The Participation of Microglia in Neurogenesis: A Review. Brain Sci. 11, 658. 10.3390/brainsci11050658. [PubMed: 34070012]
72. Santos EN, and Fields RD (2021). Regulation of myelination by microglia. Sci. Adv. 7, eabk1131. 10.1126/sciadv.abk1131. [PubMed: 34890221]
73. Mohseni-Moghaddam P, Roghani M, Khaleghzadeh-Ahangar H, Sadr SS, and Sala C (2021). A literature overview on epilepsy and inflammasome activation. Brain Res. Bull. 172, 229–235. 10.1016/j.brainresbull.2021.05.001. [PubMed: 33964347]
74. Vezzani A, and Baram TZ (2007). New Roles for Interleukin-1 Beta in the Mechanisms of Epilepsy. Epilepsy Curr. 7, 45–50. 10.1111/j.1535-7511.2007.00165.x. [PubMed: 17505552]
75. Dawson R, and Wallace DR (1992). Kainic acid-induced seizures in aged rats: neurochemical correlates. Brain Res. Bull. 29, 459–468. 10.1016/0361-9230(92)90083-a. [PubMed: 1393617]
76. Lévesque M, and Avoli M (2013). The kainic acid model of temporal lobe epilepsy. Neurosci. Biobehav. Rev. 37, 2887–2899. 10.1016/j.neubiorev.2013.10.011. [PubMed: 24184743]
77. Sharma S, Puttachary S, Thippeswamy A, Kanthasamy AG, and Thippeswamy T (2018). Status Epilepticus: Behavioral and Electroencephalography Seizure Correlates in Kainate Experimental Models. Front. Neurol. 9, 7. 10.3389/fneur.2018.00007. [PubMed: 29410648]
78. Siracusa R, Fusco R, and Cuzzocrea S (2019). Astrocytes: Role and Functions in Brain Pathologies. Front. Pharmacol. 10, 1114. 10.3389/fphar.2019.01114. [PubMed: 31611796]
79. McNeill J, Rudyk C, Hildebrand ME, and Salmaso N (2021). Ion Channels and Electrophysiological Properties of Astrocytes: Implications for Emergent Stimulation Technologies. Front. Cell. Neurosci. 15, 644126. 10.3389/fncel.2021.644126. [PubMed: 34093129]
80. Halassa MM, Fellin T, Takano H, Dong J-H, and Haydon PG (2007). Synaptic Islands Defined by the Territory of a Single Astrocyte. J. Neurosci. 27, 6473–6477. 10.1523/JNEUROSCI.1419-07.2007. [PubMed: 17567808]
81. Chung W-S, Allen NJ, and Eroglu C (2015). Astrocytes Control Synapse Formation, Function, and Elimination. Cold Spring Harb. Perspect. Biol. 7, a020370. 10.1101/cshperspect.a020370. [PubMed: 25663667]
82. Yona S, Kim K-W, Wolf Y, Mildner A, Varol D, Breker M, Strauss-Ayali D, Viukov S, Guilliams M, Misharin A, et al. (2013). Fate mapping reveals origins and dynamics of monocytes and tissue macrophages under homeostasis. Immunity 38, 79–91. 10.1016/j.immuni.2012.12.001. [PubMed: 23273845]
83. Butler A, Hoffman P, Smibert P, Papalexi E, and Satija R (2018). Integrating single-cell transcriptomic data across different conditions, technologies, and species. Nat. Biotechnol. 36, 411–420. 10.1038/nbt.4096. [PubMed: 29608179]
84. Stuart T, Butler A, Hoffman P, Hafemeister C, Papalexi E, Mauck WM, Hao Y, Stoeckius M, Smibert P, and Satija R (2019). Comprehensive Integration of Single-Cell Data. Cell 177, 1888–1902. e21. 10.1016/j.cell.2019.05.031. [PubMed: 31178118]
85. Feng G, Mellor RH, Bernstein M, Keller-Peck C, Nguyen QT, Wallace M, Nerbonne JM, Lichtman JW, and Sanes JR (2000). Imaging neuronal subsets in transgenic mice expressing multiple spectral variants of GFP. Neuron 28, 41–51. 10.1016/s0896-6273(00)00084-2. [PubMed: 11086982]

86. Porrero C, Rubio-Garrido P, Avendaño C, and Clascá F (2010). Mapping of fluorescent protein-expressing neurons and axon pathways in adult and developing Thy1-eYFP-H transgenic mice. Brain Res. 1345, 59–72. 10.1016/j.brainres.2010.05.061. [PubMed: 20510892]

87. Oakley H, Cole SL, Logan S, Maus E, Shao P, Craft J, Guillozet-Bongaarts A, Ohno M, Disterhoft J, Van Eldik L, et al. (2006). Intraneuronal beta-amyloid aggregates, neurodegeneration, and neuron loss in transgenic mice with five familial Alzheimer's disease mutations: potential factors in amyloid plaque formation. J. Neurosci. 26, 10129–10140. 10.1523/JNEUROSCI.1202-06.2006. [PubMed: 17021169]

88. Kuida K, Lippke JA, Ku G, Harding MW, Livingston DJ, Su MS, and Flavell RA (1995). Altered cytokine export and apoptosis in mice deficient in interleukin-1 beta converting enzyme. Science 267, 2000–2003. 10.1126/science.7535475. [PubMed: 7535475]

89. Allen WE, DeNardo LA, Chen MZ, Liu CD, Loh KM, Fenno LE, Ramakrishnan C, Deisseroth K, and Luo L (2017). Thirst-associated preoptic neurons encode an aversive motivational drive. Science 357, 1149–1155. 10.1126/science.aan6747. [PubMed: 28912243]

90. DeNardo LA, Liu CD, Allen WE, Adams EL, Friedmann D, Fu L, Guenthner CJ, Tessier-Lavigne M, and Luo L (2019). Temporal evolution of cortical ensembles promoting remote memory retrieval. Nat. Neurosci. 22, 460–469. 10.1038/s41593-018-0318-7. [PubMed: 30692687]

91. Madisen L, Zwingman TA, Sunkin SM, Oh SW, Zariwala HA, Gu H, Ng LL, Palmiter RD, Hawrylycz MJ, Jones AR, et al. (2010). A robust and high-throughput Cre reporting and characterization system for the whole mouse brain. Nat. Neurosci. 13, 133–140. 10.1038/nn.2467. [PubMed: 20023653]

92. Case CL, Kohler LJ, Lima JB, Strowig T, de Zoete MR, Flavell RA, Zamboni DS, and Roy CR (2013). Caspase-11 stimulates rapid flagellin-independent pyroptosis in response to Legionella pneumophila. Proc. Natl. Acad. Sci. USA 110, 1851–1856. 10.1073/pnas.1211521110. [PubMed: 23307811]

93. Srinivasan R, Lu T-Y, Chai H, Xu J, Huang BS, Golshani P, Coppola G, and Khakh BS (2016). New Transgenic Mouse Lines for Selectively Targeting Astrocytes and Studying Calcium Signals in Astrocyte Processes In Situ and In Vivo. Neuron 92, 1181–1195. 10.1016/j.neuron.2016.11.030. [PubMed: 27939582]

94. Zhu Y, Romero MI, Ghosh P, Ye Z, Charnay P, Rushing EJ, Marth JD, and Parada LF (2001). Ablation of NF1 function in neurons induces abnormal development of cerebral cortex and reactive gliosis in the brain. Genes Dev. 15, 859–876. 10.1101/gad.862101. [PubMed: 11297510]

95. Bunton-Stasyshyn RKA, Wagnon JL, Wengert ER, Barker BS, Faulkner A, Wagley PK, Bhatia K, Jones JM, Maniaci MR, Parent JM, et al. (2019). Prominent role of forebrain excitatory neurons in SCN8A encephalopathy. Brain 142, 362–375. 10.1093/brain/awy324. [PubMed: 30601941]

96. Ottolini M, Barker BS, Gaykema RP, Meisler MH, and Patel MK (2017). Aberrant Sodium Channel Currents and Hyperexcitability of Medial Entorhinal Cortex Neurons in a Mouse Model of SCN8A Encephalopathy. J. Neurosci. 37, 7643–7655. 10.1523/JNEUROSCI.2709-16.2017. [PubMed: 28676574]

97. Wengert ER, Miralles RM, Wedgwood KCA, Wagley PK, Strohm SM, Panchal PS, Idrissi AM, Wenker IC, Thompson JA, Gaykema RP, et al. (2021). Somatostatin-Positive Interneurons Contribute to Seizures in SCN8A Epileptic Encephalopathy. J. Neurosci. 41, 9257–9273. 10.1523/JNEUROSCI.0718-21.2021. [PubMed: 34544834]

98. Bolte AC, Dutta AB, Hurt ME, Smirnov I, Kovacs MA, McKee CA, Ennerfelt HE, Shapiro D, Nguyen BH, Frost EL, et al. (2020). Meningeal lymphatic dysfunction exacerbates traumatic brain injury pathogenesis. Nat. Commun. 11, 4524. 10.1038/s41467-020-18113-4. [PubMed: 32913280]

99. Zengeler KE, Shapiro DA, Bruch KR, Lammert CR, Ennerfelt H, and Lukens JR (2023). SSRI treatment modifies the effects of maternal inflammation on in utero physiology and offspring neurobiology. Brain Behav. Immun. 108, 80–97. 10.1016/j.bbi.2022.10.024. [PubMed: 36343752]

Highlights

- Inflammasome activation is dynamically regulated in the healthy adult brain
- Astrocyte-specific inflammasome activity alters hippocampal plasticity
- Astrocyte-derived caspase-1 and IL-18 modulate hippocampal IL-33 production
- Astrocyte-intrinsic inflammasome signaling propagates seizure progression

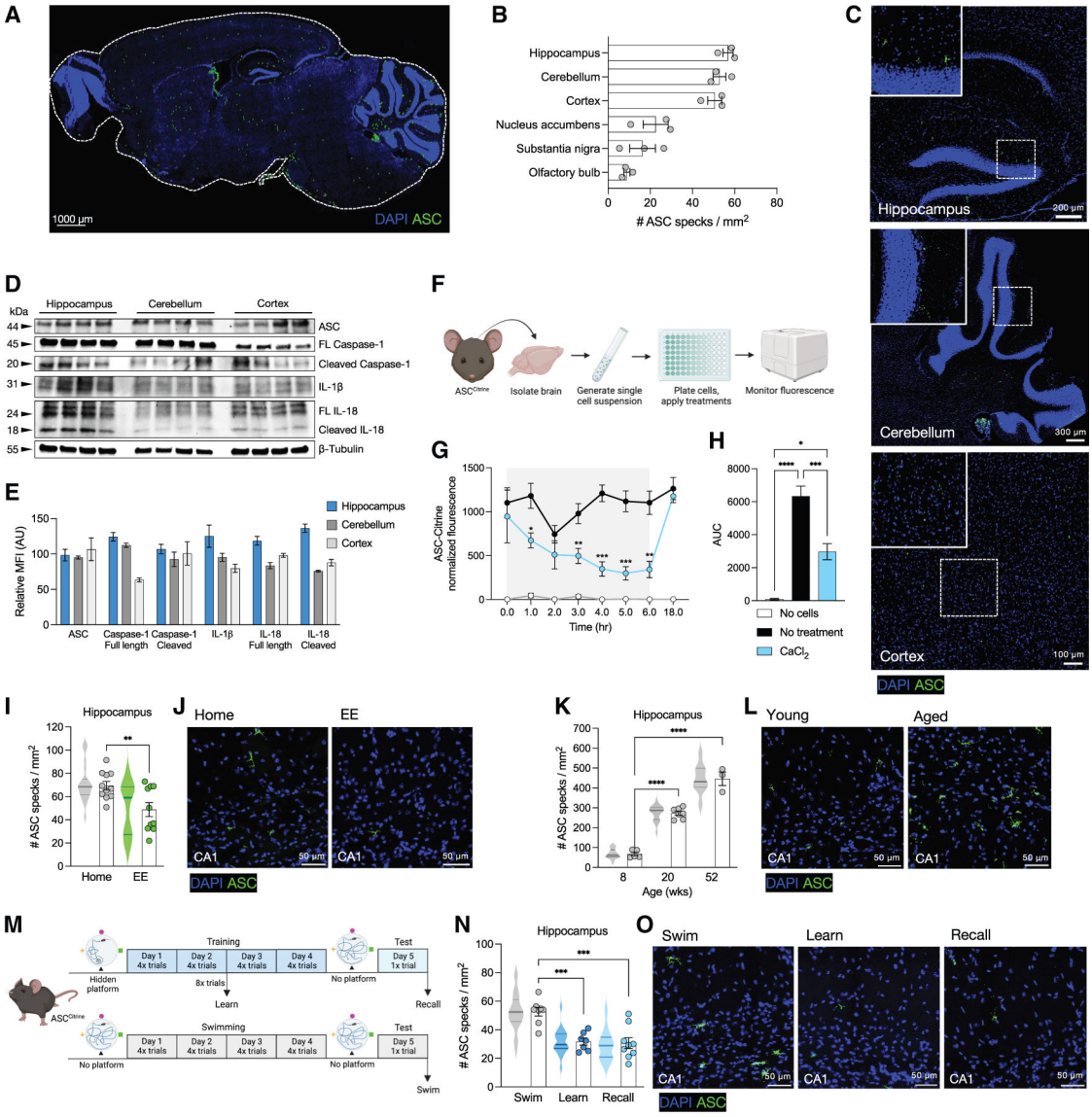

Figure 1. Inflammasome activation is dynamically regulated in the adult brain

(A) Representative brain section from an adult ASC^{Citrine} mouse. ASC specks are represented by green dots generated using Imaris software.

(B) Quantification of ASC speck density by brain region in adult ASC^{Citrine} mice.

(C) Representative images of inflammasome activation in the hippocampus (top), cerebellum (middle), and cortex (bottom) from an adult ASC^{Citrine} mouse. Insets show magnification.

(D and E) Engagement of inflammasome signaling in the adult brain assessed by western blot on microdissected hippocampus, cerebellum, and cortex WT lysates.

(D) Representative blots. FL, full length.

(E) Quantification of relative protein abundance. Signal mean fluorescence intensity (MFI) was measured across all bands (in arbitrary units [a.u.]) then percent of total signal was calculated for each band ($n = 4$).

(F–H) Citrine fluorescence in primary $ASC^{Citrine}$ CNS cells in response to $CaCl_2$ (2 mM) applied for 6 h. Treatment was washed out overnight and fluorescence read again at 18 h. (F) Experimental design. (G) $ASC^{Citrine}$ fluorescence over time normalized to background signal. The gray box indicates the treatment window. (H) Area under the curve (AUC) of $ASC^{Citrine}$ fluorescence from 0 to 6 h. Data combined from 4 to 6 wells per group. (I–L) $ASC^{Citrine}$ mice (8–12 weeks old) were exposed to an EE for 48 h (I and J) or left to age (K and L). Control mice were left in their home cages. (I and K) Quantification of the number of ASC specks over the entire hippocampus. (J and L) Representative CA1 images. (M–O) Adult (8–12 weeks old) $ASC^{Citrine}$ mice were trained on the MWM and brains were harvested immediately following 2 days of training (learn group) or after the probe trial (recall group). Mice that underwent the same treatment but without a hidden platform were used as controls and harvested following the probe trial (swim group). (M) Experimental design. (N) Quantification of the number of ASC specks over the entire hippocampus. (O) Representative CA1 images. Violin plots represent quantification per image and dots represent average data per an individual mouse. Error bars represent mean ± SEM. Statistical significance calculated by mixed effects analysis (G), one-way ANOVA with Tukey's multiple comparisons test (H), or using linear mixed effects modeling (I, K, and N). *$p < 0.05$, **$p < 0.01$, ***$p < 0.001$, ****$p < 0.0001$. See also Figure S1.

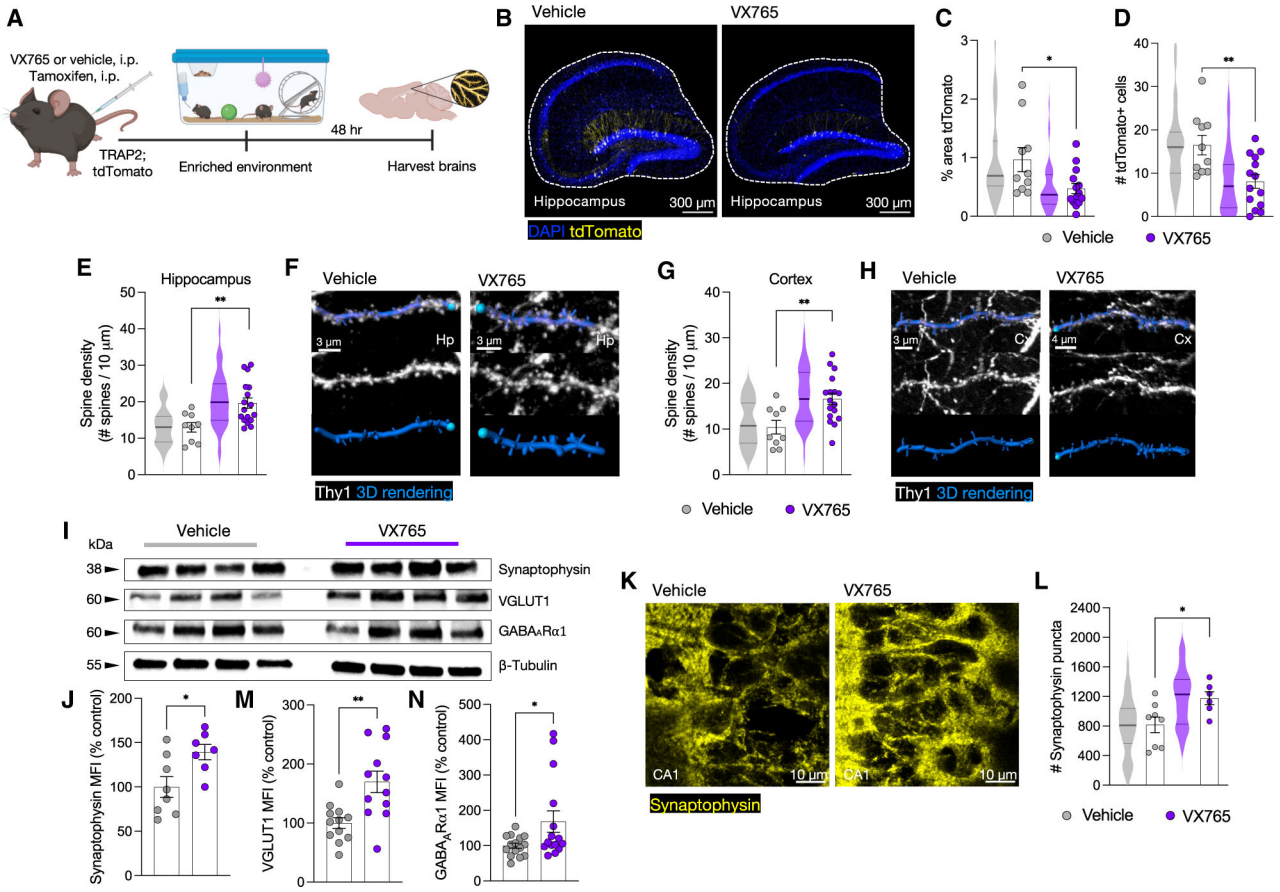

Figure 2. Caspase-1 inhibition alters neuronal plasticity

(A–D) Adult TRAP2;tdTomato mice were injected intraperitoneal (i.p.) with 50 mg/kg VX765 or vehicle control, left to rest for 10 min, and then injected with 150 mg/kg tamoxifen. After 30 min, mice were placed into an EE for 48 h, followed by brain harvesting for immunofluorescence. (A) Experimental design. (B–D) Hippocampal trapped tdTomato analysis. (B) Representative images. Quantification of the percent area of total hippocampal coverage of tdTomato+ area (C) and total count of tdTomato+ neurons (D).

(E–N) Adult Thy1^{YFP} mice were treated with 30 mg/kg VX765 or vehicle control by i.p. injection 3×/week until harvesting. (E–H) Neuronal spines in the hippocampus (Hp; E and F) and cortex (Cx; G and H) of vehicle- or VX765-treated mice were 3D reconstructed using Imaris software. (E and G) Quantification of average spine density (number of spines per 10 μm). (F and H) Representative images and 3D renderings. (I, J, M, and N) Synaptophysin, VGLUT1, and $GABA_AR\alpha1$ protein assessed by western blot on hippocampal lysates from vehicle- or VX765-treated mice. (I) Representative blots. Quantification of MFI of synaptophysin (J), VGLUT1 (M), and $GABA_AR\alpha1$ (N) normalized to percent of the control samples for each blot. (K and L) Immunohistochemistry of synaptophysin in hippocampal CA1. (K) Representative images. (L) Quantification of the number of synaptophysin puncta per field of view (FOV). Violin plots represent quantification per image and dots represent average data per an individual mouse. Error bars represent mean ± SEM. Statistical significance calculated using linear mixed effects modeling (C–E, G, and L) or by unpaired Student's t test (J, M, and N). *$p < 0.05$, **$p < 0.01$. See also Figure S2.

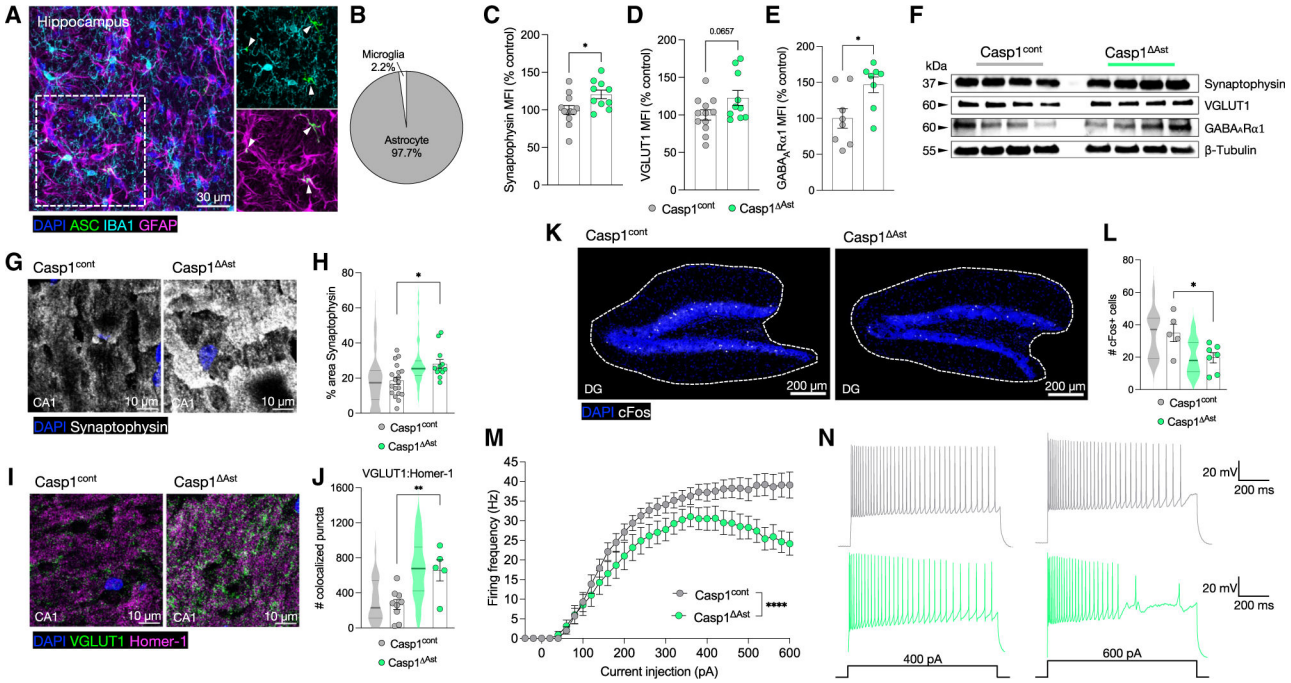

Figure 3. Astrocyte-specific inflammasome activity influences neuronal plasticity

(A and B) Inflammasome cell-type localization in the hippocampus of ASC^{Citrine} mice. (A) Representative images. Images to the right show distinct colocalized channels within the area of the dotted box to the left. White arrows point to ASC specks. (B) Pie chart depicting the relative presence of ASC specks within astrocytes (GFAP+ cells) compared with microglia (IBA1+ cells) divided by the total number of ASC specks in a FOV. 3–5 FOVs analyzed per mouse (n = 3 mice).

(C–L) Brains were harvested from Casp1$^{\Delta Ast}$ and Casp1^{cont} mice at 4–6 months of age for western blot on hippocampal lysates (C–F) and hippocampal CA1 immunohistochemistry (G–L). Quantification of MFI of synaptophysin (C), VGLUT1 (D), and GABA$_A$Rα1 (E) normalized to percent of the control samples for each blot. (F) Representative blots. (G) Representative images and (H) quantification of the percent area of synaptophysin coverage per FOV. (I) Representative images and (J) quantification of the number of VGLUT1 and Homer-1 puncta colocalized per FOV. (K) Representative images from hippocampal DG and (L) quantification of the total number of c-Fos+ puncta per hippocampus.

(M and N) Whole-cell electrophysiology recordings were conducted in slices from male mice (8–12 weeks) in Casp1^{cont} (n = 11, 5) and Casp1$^{\Delta Ast}$ (n = 9, 3) CA1 neurons (n = cells, animals). (M) Average number of action potentials elicited relative to current injection steps. (N) Representative traces of neuronal firing at 400 and 600 pA current injections for Casp1^{cont} (top) and Casp1$^{\Delta Ast}$ (bottom) CA1 neurons. Violin plots represent quantification per image and dots represent average data per an individual mouse (C–E, H, J, and L) or the average of all mice per group (M). Error bars represent mean ± SEM. Statistical significance calculated by unpaired Student's t test (C–E), linear mixed effects modeling (H, J, and L), or Kolmogorov-Smirnov test (M). *p < 0.05, **p < 0.01, ****p < 0.001. See also Figures S2 and S3.

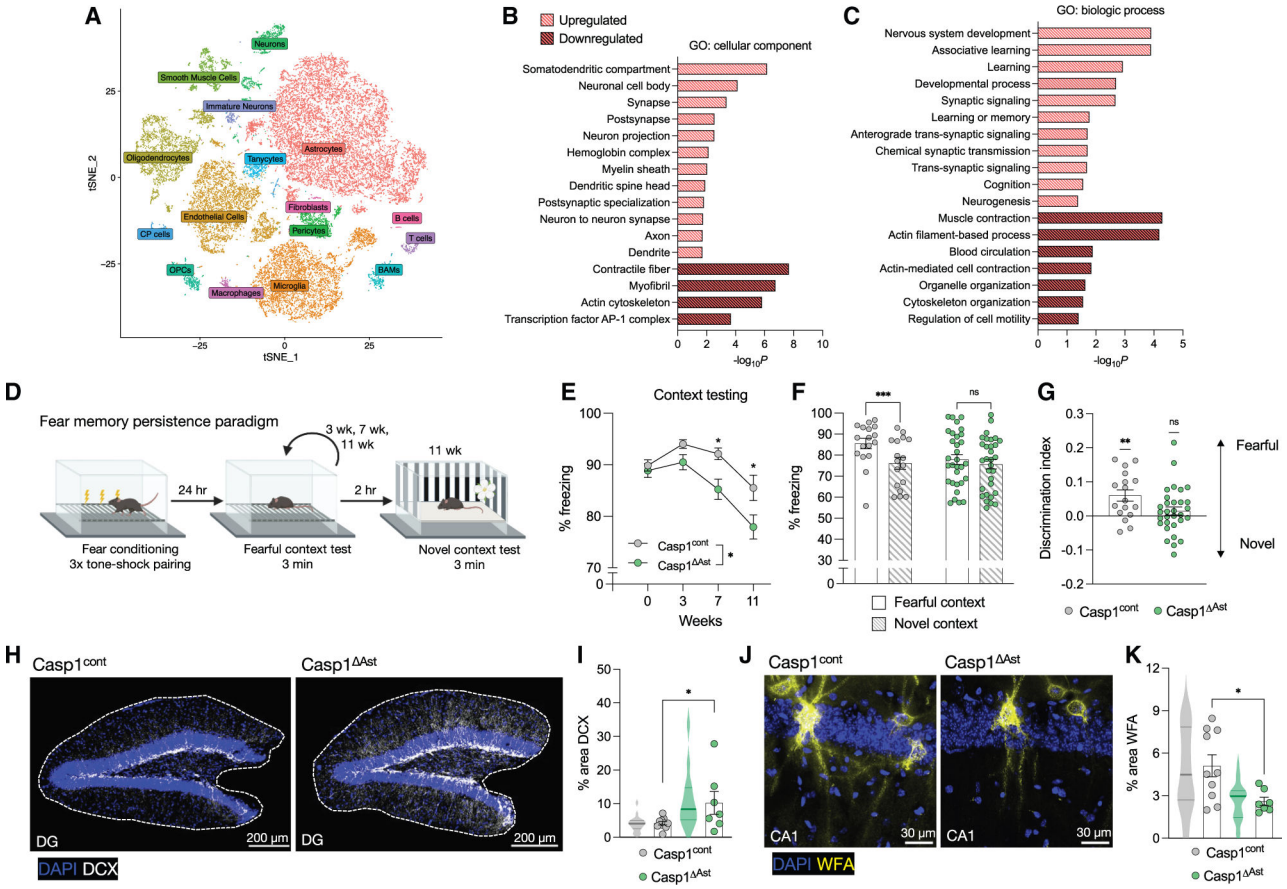

Figure 4. Caspase-1 signaling in astrocytes regulates hippocampal function, neurogenesis, and PNNs

(A–C) Hippocampi from Casp1$^{\Delta Ast}$ and Casp1^{cont} mice (n = 3 per group) were harvested at 14 weeks of age for scRNA-seq. (A) tSNE plot representing the cell types retrieved from Casp1^{cont} and Casp1$^{\Delta Ast}$ hippocampi. BAMs, border-associated macrophages; OPCs, oligodendrocyte progenitor cells; CP cells, choroid plexus cells. (B and C) Bar charts representing select GO terms collected from upregulated and downregulated genes between all hippocampal cells. (B) Cellular component and (C) biologic process GO terms.

(D–G) Memory function assessed in adult Casp1$^{\Delta Ast}$ and Casp1^{cont} mice using a fear conditioning memory persistence paradigm. (D) Experimental design. (E) Percent time spent immobile (freezing) during the context test assessed on consecutive test sessions. (F and G) At the 11-week test session, mice were also exposed to a novel, untrained context. (F) The percent time spent immobile (freezing) during the exposure to the trained (“fearful”) context compared with the untrained (“novel”) context. (G) Memory discrimination between trained and novel contexts.

(H–K) Brains of Casp1$^{\Delta Ast}$ and Casp1^{cont} mice were harvested at 4–6 months of age for immunohistochemistry. (H) Representative images and (I) quantification of the percent area of DCX coverage in hippocampal DG. (J) Representative images and (K) quantification of the percent area of WFA coverage in hippocampal CA1. Violin plots represent quantification per image and dots represent average data per an individual mouse (F, G, I, and K) or the average of all mice per group (E). Error bars represent mean ± SEM. Statistical significance

calculated by mixed effects analysis with Šídák's multiple comparisons test (E), two-way ANOVA with Šídák's multiple comparisons test (F), one-sample t test with Wilcoxon test against zero (G), or linear mixed effects modeling (I and K). *$p < 0.05$, **$p < 0.01$, ***$p < 0.001$, ns = not significant. See also Figures S3–S5.

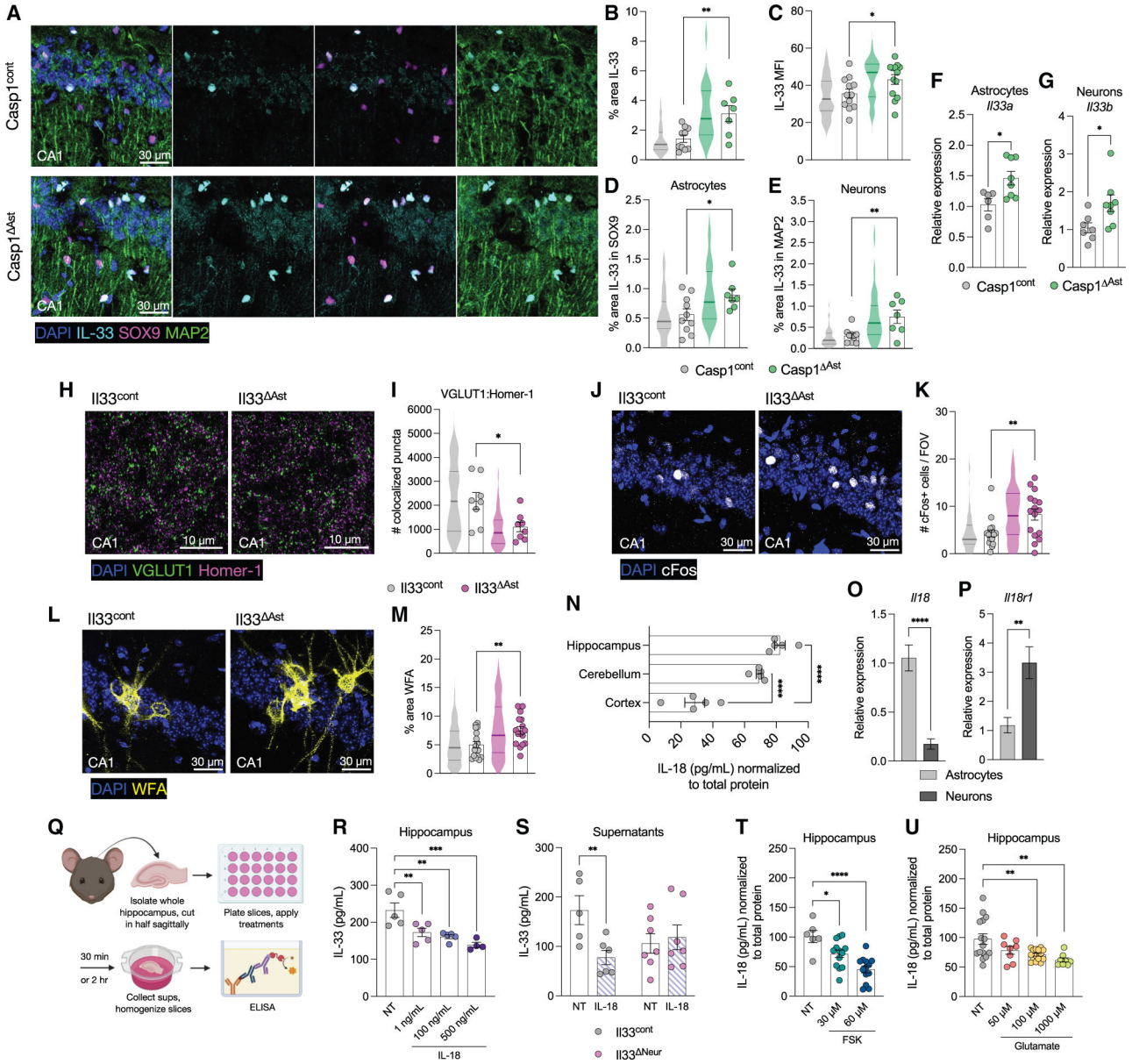

Figure 5. Astrocyte inflammasome signaling modulates IL-33-related hippocampal plasticity

Brains were harvested from Casp1$^{\Delta Ast}$, Il33$^{\Delta Ast}$, Il33$^{\Delta Neur}$, and respective Cre-negative littermate controls (Casp1^{cont} and Il33^{cont}) at 4–6 months of age.

(A–E) Relative IL-33 protein in astrocytes (SOX9+ cells) and neurons (MAP2+ cells) in hippocampal CA1 of Casp1^{cont} and Casp1$^{\Delta Ast}$ mice by immunohistochemistry. (A) Representative images. Quantification of (B) percent area coverage and (C) MFI of IL-33 signal per FOV. Quantification of IL-33 within thresholded SOX9+ (D) or MAP2+ (E) area plotted as a percent of total IL-33 signal per FOV.

(F and G) *Il33* transcriptional expression in Casp1$^{\Delta Ast}$ and Casp1^{cont} mice relative to *Gapdh*. (F) Expression of *Il33a* in sorted astrocytes. (G) Expression of *Il33b* in sorted neurons.

(H–M) Immunohistochemistry in hippocampal CA1 of Il33$^{\Delta Ast}$ and Il33^{cont} mice. (H) Representative images and (I) quantification of the number of colocalized VGLUT1 and

Homer-1 puncta per FOV. (J) Representative images and (K) quantification of the total number of c-Fos+ puncta per FOV. (L) Representative images and (M) quantification of WFA percent area coverage per FOV.

(N) Relative IL-18 concentration by ELISA in microdissected hippocampus, cerebellum, and cortex lysates from adult WT mice.

(O and P) Relative expression of *Il18* (O) and *Il18r1* (P) in sorted neurons and astrocytes from Casp1^{cont} mice (O: astrocyte $n = 7$, neuron $n = 7$; P: astrocyte $n = 7$, neuron $n = 3$).

(Q–U) Primary halved hippocampi isolated from Casp1^{cont} mice (R, T, and U) or Il33$^{\Delta Neur}$ and Il33^{cont} mice (S) exposed to treatments then homogenized for IL-33 (R and S) or IL-18 (T and U) ELISA. (Q) Experimental design. (R) Hippocampal lysate IL-33 concentration under increasing IL-18 (1, 100, or 500 ng/mL) treatments applied for 30 min. (S) Supernatant IL-33 concentration after 2 h treatment with 100 ng/mL IL-18. (T and U) Relative IL-18 concentration normalized to total protein per hippocampus slice under increasing forskolin (FSK; 30 or 60 μM; T) or glutamate (50, 100, or 1,000 μM; U) concentrations. Violin plots represent quantification per image and dots represent average data per an individual mouse. Error bars represent mean ± SEM. Statistical significance calculated using linear mixed effects modeling (B–E, I, K, and M), unpaired Student's t test (F, G, O, and P), one-way ANOVA with Tukey's multiple comparisons test (N), one-way ANOVA with Dunnett's multiple comparisons test (R, T, and U), or mixed effects analysis with uncorrected Fisher's least significant difference test (S). *$p < 0.05$, **$p < 0.01$, ***$p < 0.001$, ****$p < 0.0001$. See also Figures S5 and S6.

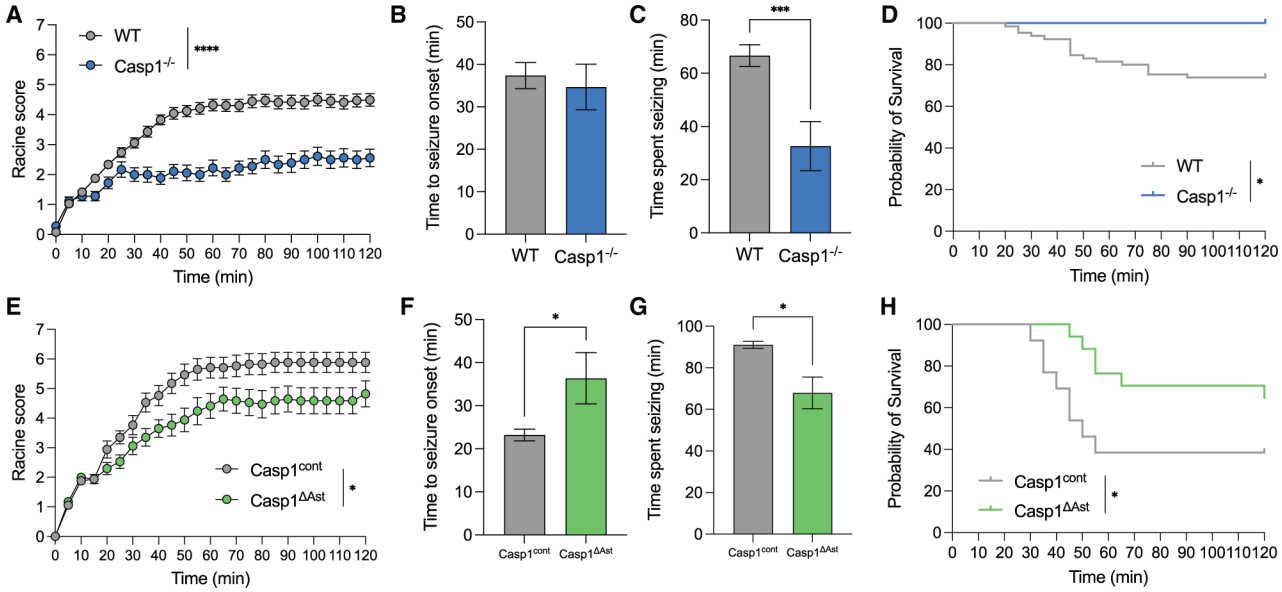

Figure 6. Inflammasome activation propagates seizure progression

Mice (6 weeks old) were injected i.p. with KA and then scored for 2 h using a modified Racine seizure scale.

(A–D) Male and female WT ($n = 65$) and Casp1$^{-/-}$ ($n = 18$) mice were injected with 24 mg/kg KA.

(E–H) Casp1^{cont} ($n = 17$) and Casp1$^{\Delta Ast}$ ($n = 17$) mice were injected with 16 mg/kg KA.

(A and E) Seizure activity scored every 5 min.

(B and F) Time to seizure onset (Racine score 3) for mice that actively seized during the 2 h scoring time.

(C and G) Time spent seizing represented by sum of time from reaching Racine score of 4 until end of scoring period.

(D and H) Survival curve. Data combined from at least three independent experiments. Each data point represents the average of every mouse within the group (A and E). Error bars indicate mean ± SEM. Statistical significance calculated by two-way ANOVA (A and E), unpaired Student's t test (B, C, F, and G), or Gehan-Breslow-Wilcoxon test (D and H). *$p < 0.05$, ***$p < 0.001$, ****$p < 0.0001$. See also Figure S6.

KEY RESOURCES TABLE

REAGENT or RESOURCE	SOURCE	IDENTIFIER
Antibodies		
Rabbit monoclonal anti-Aldh1l1 (clone E7I2Q)	Cell Signaling	Cat# 85828; RRID:AB_3065208
Rabbit polyclonal anti-ASC (clone AL177)	AdipoGen	Cat# AG-25B-0006-C100; RRID:AB_2490442
Rabbit polyclonal anti-Calbindin (clone D-28K)	Millipore Sigma	Cat# PC253L; RRID:AB_213554
Rat monoclonal anti-CD68 (clone FA-11)	BioRad	Cat# MCA1957T; RRID:AB_2074849
Rabbit polyclonal anti-c-Fos	Abcam	Cat# ab190289; RRID:AB_2737414
Rat monoclonal anti-GFAP (clone 2.2B10)	Invitrogen	Cat# 13-0300: RRID:AB_86543
Rabbit monoclonal anti-GSDMD (clone EPR19828)	Abcam	Cat# ab209845; RRID:AB_2783550
Rabbit polyclonal anti-Homer-1	Synaptic Systems	Cat# 160 003; RRID:AB_887730
Goat polyclonal anti-Iba1	Abcam	Cat# ab5076; RRID:AB_2224402
Goat polyclonal anti-IL-33	R&D Systems	Cat# AF3626: RRID:AB_884269
Rat monoclonal anti-Ki67 Alexa Fluor 660 (clone SolA15)	Invitrogen	Cat# 606-5698-82; RRID:AB_2896286
Mouse monoclonal anti-MAP2 (clone M13)	Invitrogen	Cat# 13-1500; RRID:AB_2533001
Mouse monoclonal anti-NeuN biotin-conjugated (clone A60)	Millipore Sigma	Cat# MAB377B; RRID:AB_177621
Rabbit polyclonal anti-P2RY12	AnaSpec	Cat# AS-55043A; RRID:AB_2298886
Rabbit polyclonal anti-S100β	Proteintech	Cat# 15146-1-AP; RRID:AB_2254244
Rabbit monoclonal anti-SOX9 (clone EPR14335-78)	Abcam	Cat# ab185966: RRID:AB_2728660
Guinea pig polyclonal anti-Synapsin1/2	Synaptic Systems	Cat# 106 004; RRID:AB_1106784
Rabbit polyclonal anti-Synaptophysin	Abcam	Cat# ab32594; RRID:AB_778204
Rabbit monoclonal anti-Synaptophysin (clone SP11)	Abcam	Cat# ab16659; RRID:AB_443419
Mouse monoclonal anti-VGLUT1 (clone 317G6)	Synaptic Systems	Cat# 135 511; RRID:AB_887879
Rabbit monoclonal anti-AIM2 (clone D5X7K)	Cell Signaling	Cat# 12948S; RRID:AB_2798067
Mouse monoclonal anti-Caspase-1 (Casper-1)	AdipoGen	Cat# AG-20B-0042-C100; RRID:AB_2490248
Rabbit monoclonal anti-β-Tubulin HRP Conjugate (clone 9F3)	Cell Signaling	Cat# 5346; RRID:AB_1950376
Mouse monoclonal anti-$GABA_AR\alpha1$ (clone N95/35)	Antibodies Inc	Cat# 75-136; RRID:AB_2108811
Rabbit polyclonal anti-GSDMD (clone 126–138)	Millipore Sigma	Cat# G7422; RRID:AB_1850381
Rabbit polyclonal anti-IκBα	Cell Signaling	Cat# 9242L; RRID:AB_331623
Rabbit monoclonal anti-IL-1β (clone D3H1Z)	Cell Signaling	Cat# 12507S; RRID:AB_2721117
Rabbit monoclonal anti-IL-18 (clone D2F3B)	Cell Signaling	Cat# 54943S; RRID:AB_2909592
Rabbit monoclonal anti-Phospho-NF-κB p65 (Ser536) (clone 93H1)	Cell Signaling	Cat# 3033S; RRID:AB_331284
Rabbit monoclonal anti-Phospho-IκBα (Ser32) (clone 14D4)	Cell Signaling	Cat# 2859L; RRID:AB_561111
Rabbit monoclonal anti-NF-κB p65 (clone D14E12)	Cell Signaling	Cat# 8242S; RRID:AB_10859369
Rabbit polyclonal anti-NLRP1	Proteintech	Cat# 12256-1-AP; RRID:AB_2298504
Rabbit polyclonal anti-NLRP2	Proteintech	Cat# 15182-1-AP; RRID:AB_2298531
Rabbit monoclonal anti-NLRP3 (clone D4D8T)	Cell Signaling	Cat# 15101S; RRID:AB_2722591
Anti-rabbit IgG HRP-linked	Cell Signaling	Cat# 7074P2; RRID:AB_2099233
Anti-mouse IgG HRP-linked	Cell Signaling	Cat# 7076S; RRID:AB_330924

REAGENT or RESOURCE	SOURCE	IDENTIFIER
Chemicals, peptides, and recombinant proteins		
VX-765, Caspase-1 Inhibitor	Apex Bio	Cat# A8238
Tamoxifen	Millipore Sigma	Cat# T5648
Kainic acid	Tocris	Cat# 7065
Tissue-Tek OCT compound	Sakura	Cat# 4583
Tissue Protein Extraction Reagent	Thermo Fisher	Cat# 78510
PhosSTOP Phosphatase Inhibitor Cocktail	Roche	Cat# 04906845001
cOmplete EDTA-Free Protease Inhibitor Cocktail	Roche	Cat# 11873580001
TRIzol	Life Technologies	Cat# 15596018
Papain	Worthington Biochemical	Cat# LS003127
DNase I	Roche	Cat# 10104159001
Percoll	Cytevia	Cat# 17-0891-02
$CaCl_2$	BioVision	Cat# B1010-100
Etoposide	Millipore Sigma	Cat# E1383
Forskolin	Tocris	Cat# 1099
L-Glutamic acid	Millipore Sigma	Cat# G1251
IL-18	Fisher Scientific	Cat# KMC0181
MACS BSA Stock Solution	Miltenyi Biotec	Cat# 130-0910376
Wisteria Floribunda Lectin, Biotinylated	Vector Laboratories	Cat# B-1355-2
NeuroTrace 500/525 Fluorescent Nissl Stain	Invitrogen	Cat# N21480
Propidium Iodide	Invitrogen	Cat# P1304MP
SSC Buffer 20x Concentrate	Millipore Sigma	Cat# S6639
RNase, DNase-free	Roche	Cat# 11119915001
ProLong Gold Antifade Mountant	Invitrogen	Cat# P36930
Ovomucoid, Trypsin Inhibitor	Worthington Biochemical	Cat# LS003087
Pierce 660 nm Protein Assay Reagent	Thermo Fisher	Cat# 22-660
4x Laemelli Sample Buffer	Bio-Rad	Cat# 1610747
SuperBlock T20 TBS Blocking Buffer	Thermo Fisher	Cat# 37536
SuperSignal West Pico PLUS Chemiluminescent Substrate	Thermo Fisher	Cat# 34580
Restore PLUS Western Blot Stripping Buffer	Thermo Fisher	Cat# 46430
Critical commercial assays		
Anti-ACSA2 MicroBead Kit, Mouse	Miltenyi Biotec	Cat# 130-097-678
Neural Tissue Dissociation Kit – Postnatal Neurons	Miltenyi Biotec	Cat# 130-094-802
Adult Neuron Isolation Kit, Mouse	Miltenyi Biotec	Cat# 130-126-603
In Situ, Cell Death Detection Kit, Fluorescein	Millipore Sigma	Cat# 11684795910
SensiFAST cDNA Synthesis Kit	Meridian Bioscience	Cat# BIO-65054
SensiFAST Probe No-ROX Kit	Meridian Bioscience	Cat# BIO-86005
SensiFAST SYBR No-ROX Kit	Meridian Bioscience	Cat# BIO-98020
Primers for *Aim2*, TaqMan gene expression assay	Thermo Fisher	Cat# Mm01295720_m1
Primers for *Casp1*, TaqMan gene expression assay	Thermo Fisher	Cat# Mm00438023_m1

REAGENT or RESOURCE	SOURCE	IDENTIFIER
Primers for *Casp1*, TaqMan gene expression assay	Thermo Fisher	Cat# Mm01243908_m1
Primers for *Gapdh*, TaqMan gene expression assay	Thermo Fisher	Cat# Mm99999915_g1
Primers for *Il1b*, TaqMan gene expression assay	Thermo Fisher	Cat# Mm00434228_m1
Primers for *Il18*, TaqMan gene expression assay	Thermo Fisher	Cat# Mm00434226_m1
Primers for *Il18r1*, TaqMan gene expression assay	Thermo Fisher	Cat# Mm00515178_m1
Primers for *Nlrp3*, TaqMan gene expression assay	Thermo Fisher	Cat# Mm00515178_m1
Primers for *Pycard*, TaqMan gene expression assay	Thermo Fisher	Cat# Mm00445747_g1
Primers for *Rbfox3*, TaqMan gene expression assay	Thermo Fisher	Cat# Mm01248781_m1
Primers for *Slc1a2*, TaqMan gene expression assay	Thermo Fisher	Cat# Mm01275814_m1
Dead Cell Removal Kit	Miltenyi Biotec	Cat# 130-090-101
Mouse IL-18 ELISA Kit	Thermo Fisher	Cat# BMS618-3
Mouse IL-33 ELISA Kit	Thermo Fisher	Cat# BMS6025
Deposited data		
Raw data from the scRNA-seq study (barcodes, features, and matrix files)	Mendeley	https://doi.org/10.17632/fwtcf2ybbn.1
All code used for bioinformatics analysis	Zenodo	doi: 10.5281/zenodo.15035204
All code used for bioinformatics analysis	GitHub	https://github.com/LukensLab/Casp1Aldh1l1-scRNAseq
Experimental models: Organisms/strains		
C57BL/6J	The Jackson Laboratory	JAX Stock no. 000664; RRID:IMSR_JAX:000664
B6.Cg-Gt(ROSA)26Sortm1.1 (CAG-Pycard/mCitrine*,-CD2*)Dtg/J	The Jackson Laboratory	JAX Stock no. 030744; RRID:IMSR_JAX:030744
B6.Cg-Tg(Thy1-YFP)HJrs/J	The Jackson Laboratory	JAX Stock no. 003782; RRID:IMSR_JAX:003782
B6.Cg-Tg(APPSwFlLon, PSEN1*M146L*L286V)6799Vas/Mmjax	The Jackson Laboratory	JAX Stock no. 034848; RRID:IMSR_JAX_034848
B6N.129S2-Casp1tm1Flv/J	The Jackson Laboratory	JAX Stock no. 016621; RRID:IMSR_JAX:016621
STOCK Fostm2.1(icre/ERT2)Luo/J	The Jackson Laboratory	JAX Stock no. 030323; RRID:IMSR_JAX:030323
B6.Cg-Gt(ROSA)26Sortm14(CAG-tdTomato)Hze/J	The Jackson Laboratory	JAX Stock no. 007914; RRID:IMSR_JAX:007914
Casp1fl/fl	Case et al.[82]	N/A
B6N.FVB-Tg(Aldh1l1-cre/ERT2)1Khakh/J	The Jackson Laboratory	JAX Stock no. 031008; RRID:IMSR_JAX:031008
B6.Cg-Tg(Syn1-cre)671Jxm/J	The Jackson Laboratory	JAX Stock no. 003966; RRID:IMSR_JAX:003966
B6J.B6N(Cg)-Cx3cr1tm1.1(cre)Jung/J	The Jackson Laboratory	JAX Stock no. 025524; RRID:IMSR_JAX:025524
Il33fi/fi	R Sharma	N/A
B6;129S6-Tg(Camk2a-cre/ERT2)1Aibs/J	The Jackson Laboratory	JAX Stock no. 012362; RRID:IMDR_JAX:012362
Oligonucleotides		

REAGENT or RESOURCE	SOURCE	IDENTIFIER
Il33a primers, SYBR Green gene expression assay	F: GCTGCAGAAGGGAGAAATCACG, R: GGAGTTGGAATACTTCATTCTAGGTCTCAT	N/A
Il33a primers, SYBR Green gene expression assay	F: GGCTCACTGCAGGAAAGTACAGCA, R: GGAGTTGGAATACTTCATTCTAGGTCTCAT	N/A
Software and algorithms		
Ethovision XT	Noldus	https://noldus.com/ethovision-xt
Rotarod (1.4.1)	MED Associates Inc	https://med-associates.com/product/rota-rod-2-software/
LAS X	Leica Microsystems	https://www.leica-microsystems.com/products/microscope-software/p/leica-las-x-ls/
Fiji	N/A	https://imagej.net/software/fiji/downloads
Imaris (9.9.1)	Oxford Instruments	https://imaris.oxinst.com/packages
MATLAB	MathWorks	https://www.mathworks.com/products/matlab.html
ClampFit (11.2)	Molecular Devices	https://www.moleculardevices.com/products/axon-patch-clamp-system
Cell Ranger	10x Genomics	https://support.10xgenomics.com/single-cell-gene-expression/software/pipelines/latest/installation
R (4.3.2 GUI 1.80 Big Sur ARM build)	N/A	https://www.r-project.org/
RStudio (2023.09.1+494).	N/A	https://posit.co/products/open-source/rstudio/
ZINB-WaVE (v1.24.0)	N/A	https://www.bioconductor.org/packages/release/bioc/html/zinbwave.html
DESeq2 (v1.42.0)	N/A	https://www.bioconductor.org/packages/release/bioc/html/DESeq2.html
Seurat	Butler et al.[83]; Stuart et al.[84]	https://satijalab.org/seurat/
EnhancedVolcano	N/A	https://www.bioconductor.org/packages/release/bioc/html/EnhancedVolcano.html
limma	N/A	https://www.bioconductor.org/packages/release/bioc/html/limma.html
scran	N/A	https://www.bioconductor.org/packages/release/bioc/html/scran.html
BiocManager, dplyr, tidyverse, ggplot2, Matrix, scales, cowplot, RCurl, ggridges, magrittr, patchwork, ggraph, clustree, metap, RColorBrewer, sctransform, openxlsx	The Comprehensive R Archive Network	https://cran.r-project.org/
GProfiler	N/A	https://biit.cs.ut.ee/gprofiler/gost
Prism (10.1.0)	GraphPad	https://www.graphpad.com/
Other		
Tamoxifen mouse chow	Envigo Teklad	Cat# TD.130858
Colored igloos	Bio-Serv	Cat# K3570, K3327

REAGENT or RESOURCE	SOURCE	IDENTIFIER
Crawl balls	Bio-Serv	Cat# K3329, K3330
Tunnels	Bio-Serv	Cat# K3322, K3323
LS Columns	Miltenyi Biotec	Cat# 130-042-401
MACS MultiStand	Miltenyi Biotec	Cat# 130-042-303
QuadroMACS Separator	Miltenyi Biotec	Cat# 130-091-051